JOURNAL OF GEOPHYSICAL RESEARCH, VOL. 104, NO. C1, PAGES 1505–1524, JANUARY 15, 1999

Geometry, migration, and evolution of wave orbital ripples at LEO-15

Peter Traykovski
Woods Hole Oceanographic Institution, Woods Hole, Massachusetts

Alex E. Hay
Department of Oceanography, Dalhousie University, Halifax, Nova Scotia, Canada

James D. Irish and James F. Lynch
Woods Hole Oceanographic Institution, Woods Hole, Massachusetts

Abstract. Observations of the temporal evolution of the geometric properties and migration of wave- formed ripples are analyzed in terms of measured suspended sand profiles and water velocity measurements. Six weeks of bedform observations were taken at the sandy (medium to coarse sized sand) LEO-15 site located on Beach Haven ridge during the late summer of 1995 with an autonomous rotary sidescan sonar. During this period, six tropical storms, several of hurricane strength, passed to the east of the study site. Ripples with wavelengths of up to 100 cm and with 15 cm amplitudes were observed. The predominant ripples were found to be wave orbital scale ripples with ripple wavelengths equal to 3/4 of the wave orbital diameter. Although orbital diameters become larger than 130 cm during the maximum wave event, it is unclear if a transition to non-orbital scaling is occurring. Ripple migration is found to be directed primarily onshore at rates of up to 80 cm/day. Suspended transport due to wave motions, calculated by multiplying acoustic backscatter measurements of suspended sand concentrations by flow velocity measurements, are unable to account for a sufficient amount of sand transport to force ripple migration and are in the opposite direction to ripple migration. Thus it is hypothesized that the onshore ripple migration is due to unobserved bedload transport or near-bottom suspended transport. Bedload model calculations forced with measured wave velocities are able to predict the magnitude and direction of transport consistent with observed ripple migration rates. Sequences of ripple pattern temporal evolution are examined showing mechanisms for ripple directional change in response to changing wave direction, as well as ripple wavelength adjustment and erosion due to changing wave orbital diameter and relative wave-to-current velocities.

1. Introduction

Bottom bedforms are an important part of the interactions between bottom boundary layer hydrodynamics and sediment transport. In particular, wave-formed ripples are the predominant bedform found in many coastal locations where the water is shallow enough to allow wave stresses to dominate over those caused by mean currents.

Previous laboratory studies such as those by *Bagnold* [1946], *Carstens et al.* [1969], *Mogridge and Kamphuis* [1972], and *Miller and Komar* [1980a] and field studies such as those by *Inman* [1957], *Dingler* [1974], and *Miller and Komar* [1980b] have led to a wealth of data on ripple geometry that has been recently reexamined by *Wiberg and Harris* [1994]. *Clifton and Dingler* [1984] identified three different classes of ripples. Orbital scale ripples have wavelengths (λ) that scale directly with the wave orbital diameter (d). Anorbital ripples have wavelengths that depend on grain size (D) alone. Suborbital ripples are a transitional stage between these two states and depend on both d and D.

Most of the previous observations have been conducted by divers, which limits the temporal sampling. Alternatively, photographic systems have been used and have been able to produce time series of ripple evolution and occasionally ripple migration rates [*Boyd et al.*, 1988]. The photographic time series measurements by *Wheatcroft* [1994], *Boyd et al.* [1988], and *Amos et al.* [1988] of the seafloor have been used to investigate the relative roles of waves and mean currents in forming different types of bedforms in varying oceanographic conditions. However, photographic systems are often unable to produce adequate images during periods of high suspended sediment concentration [*Wheatcroft*, 1994]. Recently, rotary sidescan sonar systems such as that described by *Hay and Wilson* [1994] have been used to measure bedform evolution in locations where a cable to shore is possible. We have adapted this type of sidescan sonar system for autonomous use on the continental shelf.

Paper number 1998JC900026.
0148-0227/99/1998JC900026$09.00

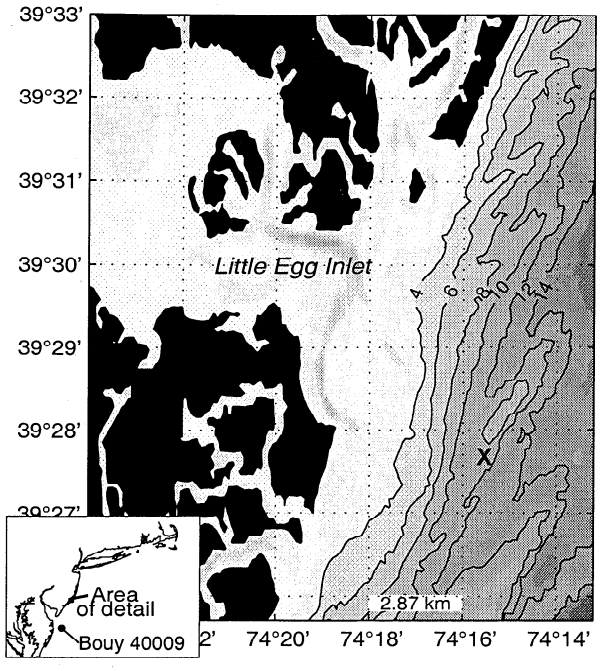

Figure 1. LEO-15 bathymetry. The tripod location on the southern end of Beach Haven ridge is marked by an X. Depth contours are labeled in meters, and the grid spacing is 2.87 km.

This rotary sidescan sonar system allows high resolution, rapid sampling of bedform morphology, and migration over extended periods. The tripod on which this sidescan sonar system was mounted also contained current meters and acoustical and optical sensors to measure sediment concentrations. This system was deployed from August 24 to September 9, 1995, at the Long Term Ecosystem Observatory (LEO-15) site off the coast of southern New Jersey (Figure 1). During this time period, six tropical storms, some of which attained hurricane strength, passed to the east of the study site. The geophysical environment at LEO-15 consists of a system of sand ridges extending north and east from the coast. The LEO-15 site is located in 11-m deep water on the southern end of Beach Haven ridge (shown as the closed contour in Figure 1). These ridges consist largely of medium sand on top of a bed of holocene lagoonal mud between the ridges [*Duane et al.*, 1972].

The purpose of this paper is to analyze these observations of bedforms in the context of previous observations of wave-formed bedforms and to relate the bedforms to the sediment transport process. The paper is organized in five sections. The first section describes the equipment deployed during this period at LEO-15 along with relevant calibration and processing information. The second section covers the evolution of ripple geometry in which observations of ripple wavelength and height are compared to previous empirical models. While most previous work has focused on ripple geometry, the sidescan sonar system is also able to resolve ripple migration rates. The third section examines ripple migration and associated sediment transport rates. The fourth section displays several individual images to illustrate mechanisms for ripple directional change, wavelength evolution and erosion. The final section places the observations in a climatological context by examining wave climatology data from the National Data Buoy Center [ftp://seaboard.ndbc.noaa.gov/data/climatic/44009.txt.gz, 1997], buoy 44009.

2. Instrumentation and Current Meter Data Processing

Since sediment transport involves the interactions of bottom boundary layer hydrodynamics, suspended sediment dynamics, and bedform morphology, it is necessary to observe all of these components. At LEO-15 a multi-instrument tripod was deployed that contained a vertical array of benthic acoustic stress sensor (BASS) [*Williams et al.*, 1987] current meters and electromagnetic current meters (EMCM) to measure water velocities, an acoustic backscattering system (ABS) to measure vertical profiles of suspended sediment concentration and local seafloor elevation, and a rotary sidescan (sector-scanning) sonar (SSS) to image bedform geometry and migration. It is worth noting that SCUBA divers reported 1- to 2-foot visibility through much of the deployment; thus it is unlikely that photographic systems would have produced adequate bedform images. Biofouling of these systems became a serious problem by the end of the deployment. Thus after yearday 260, analysis is stopped. The acoustic SSS bedform measurements were generally more robust to biofouling than the EMCM and BASS current meter measurements.

2.1. Sector-Scanning Sonar

The sector-scanning sonar images a sea-floor area of approximately 35 m^2 by projecting a beam of sound with 0.8° beam width in azimuth by 30° high in elevation on a center axis aimed 60° above vertical, as shown in Figure 2. Since the inner edge of the main beam is at an angle of 45° to the vertical, there is a region of 100 cm radius in the center that is not imaged.

The beam is rotated around through 351° in 390 0.9° steps. The range resolution of the instrument is 1 cm by sampling the envelope of the returned signal at 75 kHz. Combined with the 0.8° azimuth beam width, this gives resolution cells ranging from 1.4 x 2.0 cm at 100 cm from the center of the image to 1.1 x 5.1 cm at the maximum range of 350 cm. Photographic systems are generally able to achieve a higher resolution at the expense of sampling a smaller area. The system operates at a frequency of 2.25 MHz. Roughness features that are much larger than the acoustic wavelength of 0.66 mm scatter in the geometric regime. Since the bedform features of interest at LEO-15 have typical wavelengths of 10 to 100 cm, the images can be interpreted simply by considering

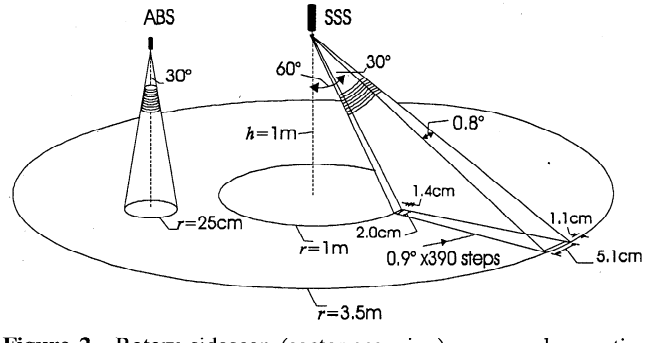

Figure 2. Rotary sidescan (sector-scanning) sonar and acoustic backscattering system.

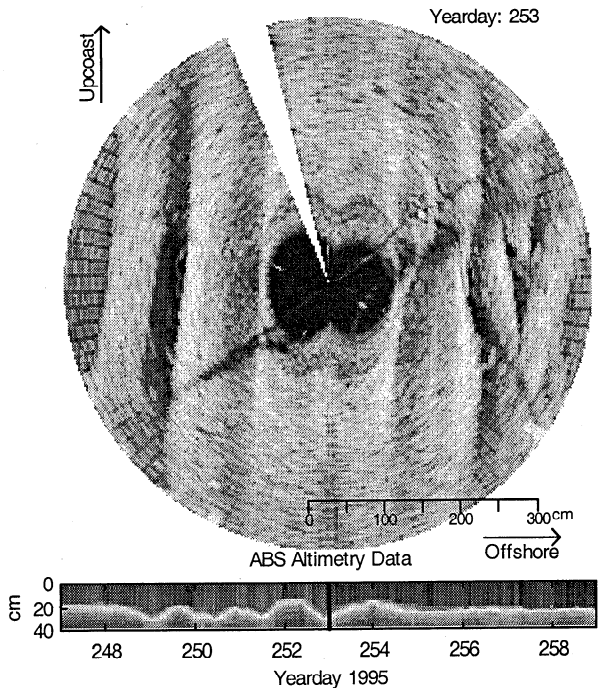

Figure 3. Sector scanning sonar image (top) and 12-day time series of ABS vertical profiler data (bottom). The sector scanner image shows some of the largest ripples observed with wavelengths of 1 m, and the ABS shows changes in seafloor elevation as the ripples migrate past the acoustic beam. Light areas in both images represent high acoustic returns. In these images the SSS was located directly over a ripple crest, while the ABS is located over a trough.

areas of high acoustic backscattered intensity (light areas in the image) as surfaces facing toward the sonar transducer head and areas of low acoustic intensity as surfaces facing away from the sonar head. This is clearly visible in the image (Figure 3) of 100-cm wavelength ripples taken on yearday 253, 1995. The acoustic shadows from the tripod legs are also noticeable in this image.

This system was originally designed by Simrad/Mesotech for use in imaging the insides of pipes and was adapted for coastal seafloor imaging applications with a cable to shore by *Hay and Wilson* [1994]. It was modified for autonomous use on the continental shelf by adding a PC 104 controller and a 2 Gb hard disk data storage system which allows sampling a new image every 30 min for a 6-week deployment such as this one conducted at LEO-15 [*Irish et al*, 1997].

2.2. Acoustic Backscattering System

The tripod contained both acoustic backscattering (ABS) and optical backscattering systems (OBS) to measure suspended sediment concentrations. The OBS system, with its maximum scattering response to sediments of radius $a\sim$ 1 μm and a^{-1} geometric scattering falloff in intensity per unit sediment volume for larger sediment sizes, is unsuitable for detecting sand in the presence of small quantities of finer sediments (Figure 4). Bottom samples reveal finer sediment in the trough adjacent to Beach Haven ridge which can be advected over the ridge by mean currents. While this suspended mud has great impact on visibility and optical backscattered (OBS) intensity it does not influence sand ripple dynamics. Therefore OBS measurements are not used in this paper. The median grain diameters (D_{50}) measured at LEO-15 are typically 1.1 to 1.6 ϕ (D_{50}~465 to 330 μm) with standard deviations of ±0.5 to ±1.0 ϕ (2 ϕ = 250 μm to 0.1 ϕ = 933 μm). Larger broken shell fragments or entire shells that generally do not compose a significant percentage of the total mass, but can occasionally skew the size statistics, were not included in the grain size analysis [*Craghan,* 1995].

The 2.5 MHz ABS system is located 110 cm above the seafloor within the imaged area of the sector-scanning sonar. It has a vertical resolution of 1 cm and a beam width of 30°, as defined by the half power points (-3 dB). The instrument sampled for 4 minutes every half hour at a rate of 2 Hz. The acoustic intensity (I) measured by this system is calibrated to give a measure of suspended sand concentration (C). This can then be multiplied by the velocity measurements to estimate suspended sediment transport rates. The return from the seafloor also gives an estimate of the local elevation. A series of ripples of 10 to 15 cm height migrating past the ABS beam are shown in Figure 2.

The ABS is calibrated in a tank with known concentrations of sediment from LEO-15 with a procedure similar to that described by *Lynch et al.* [1994]. Generally, a single-frequency acoustic system cannot measure concentration independently of sediment size since the Raleigh scattering dependence on grain size ($I/C \propto a^3$ for $ka<<1$) is stronger than the linear dependence on concentration. However, the median grain size (~400 μm) from bottom samples at LEO-15 is near the scattering maximum at $ka=1$ where k is the acoustic wavenumber (Figure 4). In this region the scattering is roughly independent of grain size, which allows the use of a single frequency concentration estimate. An estimate of the error in concentration due to uncertainty in grain size can be obtained by noting that for sediment sizes within one standard deviation of the median (light-shaded region in Figure 4) there is a maximum falloff in intensity of 50%. Thus if the median grain size of suspended sediment is within one standard deviation of the median grain size of the bottom sediment, the acoustic concentration estimates of suspended sand should be accurate to within approximately a factor of 2.

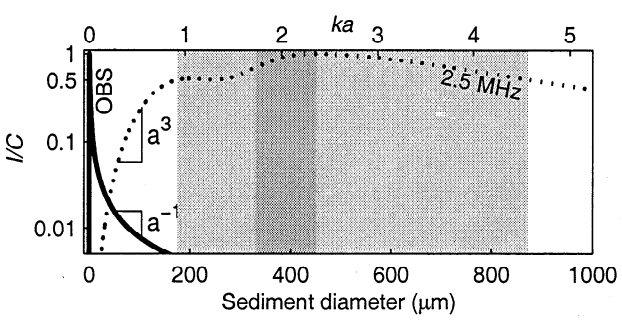

Figure 4. Acoustical and optical scattering intensities per unit sediment volume as a function of sediment diameter (D) on the bottom axis and ka on the top axis. Intensities are normalized to have a maximum of unity. The acoustic results are generated using the expressions given by *Sheng and Hay* [1988]. The range of sediment diameters for which acoustic scattering intensity is within 50% of its maximum value is lightly shaded. This is approximately equal to the median grain size ± 1 s.d. The darker-shaded region indicates the range of median grain diameters typically found at LEO-15.

2.3. Current Meters and Current Meter Data Processing

Two types of current meters were used to measure water velocities on the tripod deployed at LEO-15. A Marsh-McBirney EMCM sensor was located 500 cm above the seafloor, and a vertical array of BASS sensors were located at 44, 80, 166, and 250 cm above the seafloor. Both systems had a burst sampling rate of 4 Hz. The BASS sampled every hour with a burst length of 15 min while the EMCM sampled every 30 min for 8 min coherently with the ABS system. Since the BASS used a longer burst, the lowest BASS sensor is used to calculate burst-averaged quantities. Burst averaged root mean squared (rms) wave velocities ($u_{w,\mathrm{rms}}$) are calculated from the vector wave velocities by

$$u_{w,\mathrm{rms}} = \sqrt{\overline{|\hat{u}_w(t)|^2}}. \quad (1)$$

The overbar is used to denote burst averaged quantities throughout the paper, and the wave velocity is calculated from the two horizontal velocity axes ($\hat{u}$):

$$\hat{u}_w = \hat{u} - \hat{u}_c \quad (2)$$

where the vector mean current velocity ($\hat{u}_c$) with an alongshore component (v_c) and an across-shore component (u_c) is defined as

$$\hat{u}_c = \bar{\hat{u}} \quad (3)$$

The vector wave velocity is rotated into a coordinate system that is aligned with the dominant wave direction, and the dominant component of instantaneous wave velocity is defined as u_w. The dominant wave direction is calculated by rotating the two-axis coordinate system until the variance is maximized along one axis. The dominant wave direction does not vary more than 30° from directly onshore. Wave period ($T=2\pi/\omega$) is calculated from the energy-weighted mean frequency (ω) from the spectrum ($u^2_{w,i}$) of wave velocities by [*Madsen et al.*, 1988]

$$\omega = \frac{\sum \omega_i u^2_{w,i}}{\sum u^2_{w,i}} \quad (4)$$

Since wave orbital diameter (d_o) is an important factor for ripple geometry, it is calculated directly from the wave velocity record by first integrating u_w to get an Eulerian particle trajectory:

$$x_w(t) = \int_0^t u_w(t')dt' \quad (5)$$

This displacement time series ($x_w(t)$) is then high-pass filtered using a filter with a 22-s cutoff to keep only wave velocities and remove infragravity motions. The significant orbital diameter ($d_{o,1/3}$), which is equivalent to the orbital diameter based on significant wave height, is then calculated by

$$d_{o,1/3} = 4\sqrt{\overline{x_w^2}} \quad (6)$$

The rms orbital diameter ($d_{o,\mathrm{rms}}$, i.e., d_o based on the rms wave height) can also be calculated by $d_{o,1/3}=1.42d_{o,\mathrm{rms}}$ [*Longuet- Higgins*, 1952].

The results of these calculations for $u_{w,rms}$, T, $d_{o,1/3}$, and $\hat{u}_c$ on data from the lowest BASS sensor are shown in Figure 5. While the rms wave velocity reached peaks of 20 cm/s during the periods

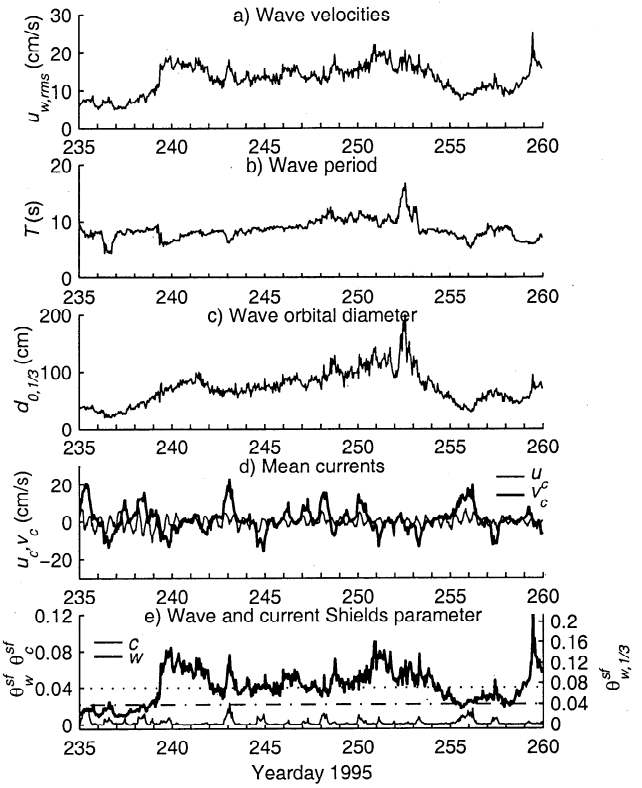

Figure 5. Current meter time series: (a) wave velocities, (b) wave period, (c) wave orbital diameters, and (d) mean currents calculated from the BASS sensor 44 cm above the seafloor. (e) Wave and current (constant drag coefficient) skin friction Shields parameter based on H_{rms} (left y-axis) and based on $H_{1/3}$ (right y-axis). The critical Shields parameter for initiation of motion of $\theta^{sf}_{\mathrm{crit}} = 0.04$ is also shown as a dash-dotted (H_{rms}) and dotted ($H_{1/3}$) line for each case.

near yearday 241 and near yearday 253, the wave period became much greater (up to 16 s) during the latter period, and thus the orbital diameter is also much larger (up to 2 m) during the latter period. Mean currents in the alongshore direction, with peaks of up to 20 cm/s, are stronger than the weaker tidal currents in the across-shore direction with peaks of 5 to 8 cm/s. The peak alongshore currents are sometimes correlated with peaks in wave velocities, for instance, near yearday 243 and 240. However, at other times, for instance near yeardays 256 and 259, there is a substantial phase lag since the waves are generated by storms located far offshore.

One of the important parameters in sediment transport that can be estimated from the current meter records is the bottom stress. The total bottom stress can be divided into a form drag component and a skin friction component, where the skin friction is primarily responsible for sediment motion. When the bottom stress due to waves is much greater than that due to current, the wave skin friction stress can estimated by:

$$\tau^{sf}_w = \frac{1}{2}\rho f_{2.5} u^2_{w,m} \quad (7)$$

Here ρ is the water density, and the wave friction factor ($f_{2.5}$) is that developed by *Swart* [1974] with the grain roughness defined by 2.5 times the median grain diameter (D_{50}). The wave velocity used in (7)

is defined by ($u_{w,m} = \sqrt{2}u_{w,\mathrm{rms}}$). Using this definition of wave velocity is equivalent to calculating wave velocity based on the rms wave height (H_{rms}). An alternate representation of the wave velocity is $u_{w,1/3} = 1.42\sqrt{2}u_{w,\mathrm{rms}}$. This calculation is consistent with using the significant wave height ($H_{1/3}$) which is also consistent with the calculation of $d_{0,1/3}$. For the purpose of determining initiation of sediment motion and predicting sediment transport, the skin friction bottom stress is often nondimensionalized by taking the ratio of the stress to the immersed weight per unit area, that is, the Shields parameter:

$$\theta_w^{sf} = \frac{\tau_w^{sf}}{\rho(s-1)gD_{50}} \tag{8}$$

where g is gravity and $s=\rho_s/\rho$ is the ratio of sediment grain density to water density.

The component of skin friction bottom stress due to the mean currents (τ_c^{sf}) was calculated in two different ways. The first method used was the Grant, Glenn and Madsen (GGM) non-linear wave current interaction bottom boundary layer model [*Grant and Madsen* 1979; *Grant and Glenn,* 1983] as described by *Madsen and Wikramanayake* [1991]. The second method was a constant drag coefficient approach as described by *Sternberg* [1972]:

$$\theta_c^{sf} = \frac{C_d|\vec{u}_{c100}|^2}{(s-1)gD_{50}} \tag{9}$$

where $\vec{u}_{c100}$ is the current velocity one meter above the seafloor found from interpolating a log velocity profile fit to the BASS vertical array of current measurements and C_d=0.003. This method was chosen since *Amos et al.* [1988] found it gave better separation of wave-versus-current dominated ripple types. The constant drag coefficient gives peak current stress estimates that are about twice that of the GGM method, while the mean ratio of the two estimates is close to 1. However, both methods show that the current stress is much weaker than the wave stress (Figure 5) with the exception of the beginning of the deployment (before yearday 239) and a period near yearday 256. On the basis of the constant drag coefficient approach, the maximum value of τ_c^{sf}/τ_w^{sf} during periods of active ripple evolution (i.e., after yearday 239) is 0.6. This value occurred near yearday 256. The mean value over the entire period from yearday 235 to 260 of this ratio is 0.09. Although the combined wave and current Shields parameter can be calculated from the vector sum of the wave and current stress, for the purposes of predicting initiation of motion it is often sufficient to consider only the wave stress since the addition of current represents a negligible difference. The primary exceptions to this occurs near yearday 255 to 256 and at the beginning of the deployment.

3. Ripple Geometry

3.1. Temporal Evolution of Ripple Characteristics and Type

Features of the evolution of ripple patterns are best displayed by examining sequences of images directly. Computer animated movies of the hourly images provide a detailed view of these processes [Traykovski, http://www.oal.whoi.edu/leo15.html]. Representative images of the different stages of ripple evolution are shown in Figure 6. Active ripple pattern changes and evolution is seen to occur throughout the period from yearday 238 to beyond yearday 260, despite the fact that θ_w^{sf}, based on H_{rms}, often dips below the critical Shields parameter of $\theta_{\mathrm{crit}}^{sf}$ = 0.04 (Figure 5). This critical Shields parameter for the initiation of motion was calculated from the modified Shields curve [*Madsen and Grant,* 1976] for sand with D_{50}=400 μm, and is consistent with the value for combined flows used by *Amos et al.* [1988] for a slightly smaller sand size (D_{50}~200μm). If the Shields parameter is instead based on $H_{1/3}$, the Shields parameter is consistently above the critical Shields parameter during the period when ripples are actively evolving. This makes physical sense because the calculations based on H_{rms} de-emphasize the contribution of the larger waves in a burst which are responsible for moving the majority of the sediment.

The deployment begins with relic ripples (Image 1), most likely left over from a strong "North Easter" storm that occurred one week prior to the deployment. The ripples have similar wavelength to actively evolving ripples on yearday 252 (Image 9), but the crests of the relic ripples were more rounded. By yearday 239.2 (Image 2) $\theta_{w,1/3}^{sf}$ has exceeded $\theta_{\mathrm{crit}}^{sf}$ and wave ripples have begun to form. These short-crested three dimensional (3-D) wave ripples are similar to the variable bifurcated ripples and chaotic ripples described by *Boyd et al.* [1988] They occur primarily as a transitional stage at the beginning of a storm event. During yearday 239 these 3-D wave ripples become more organized into long crested two dimensional (2-D) wave ripples (Image 3). This is the predominant ripple pattern seen at LEO-15 during this deployment. These are vortex ripples, as they have sharp crests that shed vortices regularly, as seen by clouds of sediment in the ABS burst data.

From yearday 240 to yearday 242 the wave direction changes through 30° from a slightly down coast direction to straight onshore. The ripples adapt to this change in wave direction by changing direction (Images 4 to 6) with a transitional stage consisting of sinuous 3-D ripples (Image 5). This sinuous pattern allows the ripple to change direction without sections migrating unreasonably long distances. By Image 6 the sinuous kinks in Image 5 have reconnected in the new direction. The crests are nearly straight and aligned with the directly onshore wave direction. While these sinuous 3-D ripples occupy a similar transitional role as the variable bifurcated ripples described by *Boyd et al.* [1988], they are generally better organized into regular patterns, with more sinuous continuous crests, and fewer crest bifurcations. *Lee Young and Sleath* [1990] presented a model for serpentine (sinuous) ripples based on the interaction of waves and mean currents from an oscillating tray flume experiment. Here a similar ripple pattern is generated by the changing wave direction. However, the fundamental physics of vorticity being swept along the ripple crest presented by *Lee Young and Sleath* [1990] may be quite similar in both mechanisms of serpentine ripple formation. A simple physical model for the wavelength of the along-crest oscillations generated as the ripple change direction is shown in Figure 7. From the intersection of the two ripple patterns the along-crest wave length p can be found to be

$$p = \sqrt{\frac{\lambda_1^2 + \lambda_2^2 + 2\lambda_1\lambda_2\cos(\theta)}{\sin^2\theta}} \tag{10}$$

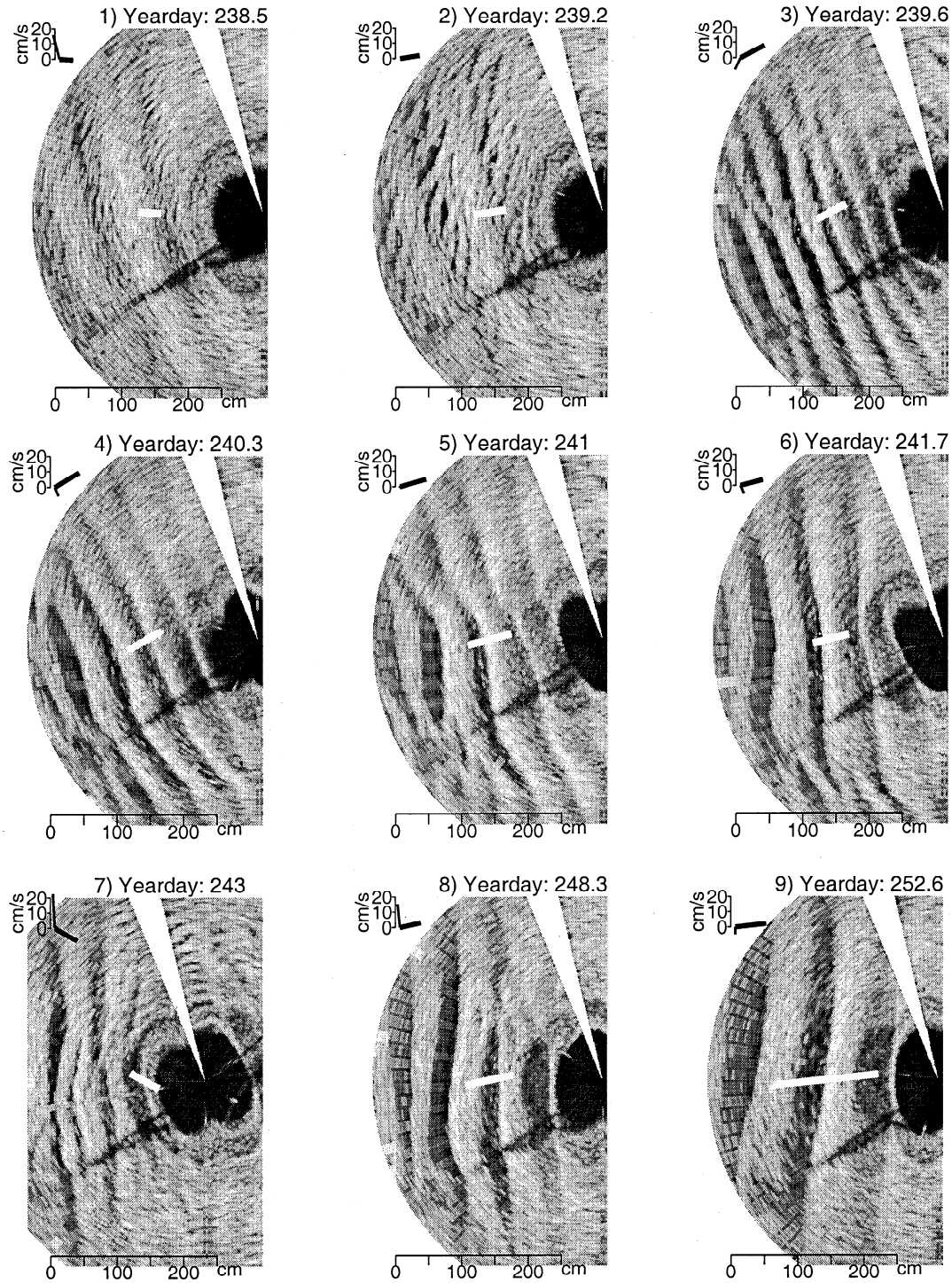

Figure 6. Representative sector-scanning sonar images. The thick white line near the center of each image represents the wave orbital diameter scaled by 3/4 and is aligned in the wave direction. The small plot below the upper left of each image displays the relative wave rms velocity (thick line) and current velocity (thin line).

For example, during the period yearday 240.3 to 241.7 (Figure 6, Image 4 through 6) the ripples turned through 30° while changing wavelength from $\lambda_1 = 50$ cm to $\lambda_2 = 70$ cm. Equation (10) predicts an along crest oscillation wavelength of p=232 cm while the measured value from Image 5 is 220 cm.

On yearday 243 the largest alongshore currents of the deployment are present and small current ripples are visible in the troughs of the wave ripples (Image 7, particularly near the missing sector of the image). Because of the sector scanner geometry, these ripples are only imaged when the acoustic beam points perpendicular to their crests. Presumably, these current ripples are also present in the troughs of all the wave ripples. *Amos et al.* [1988] presented a classification of wave versus current ripple domination in terms of θ_w^{sf} and θ_c^{sf}. In this case the values of

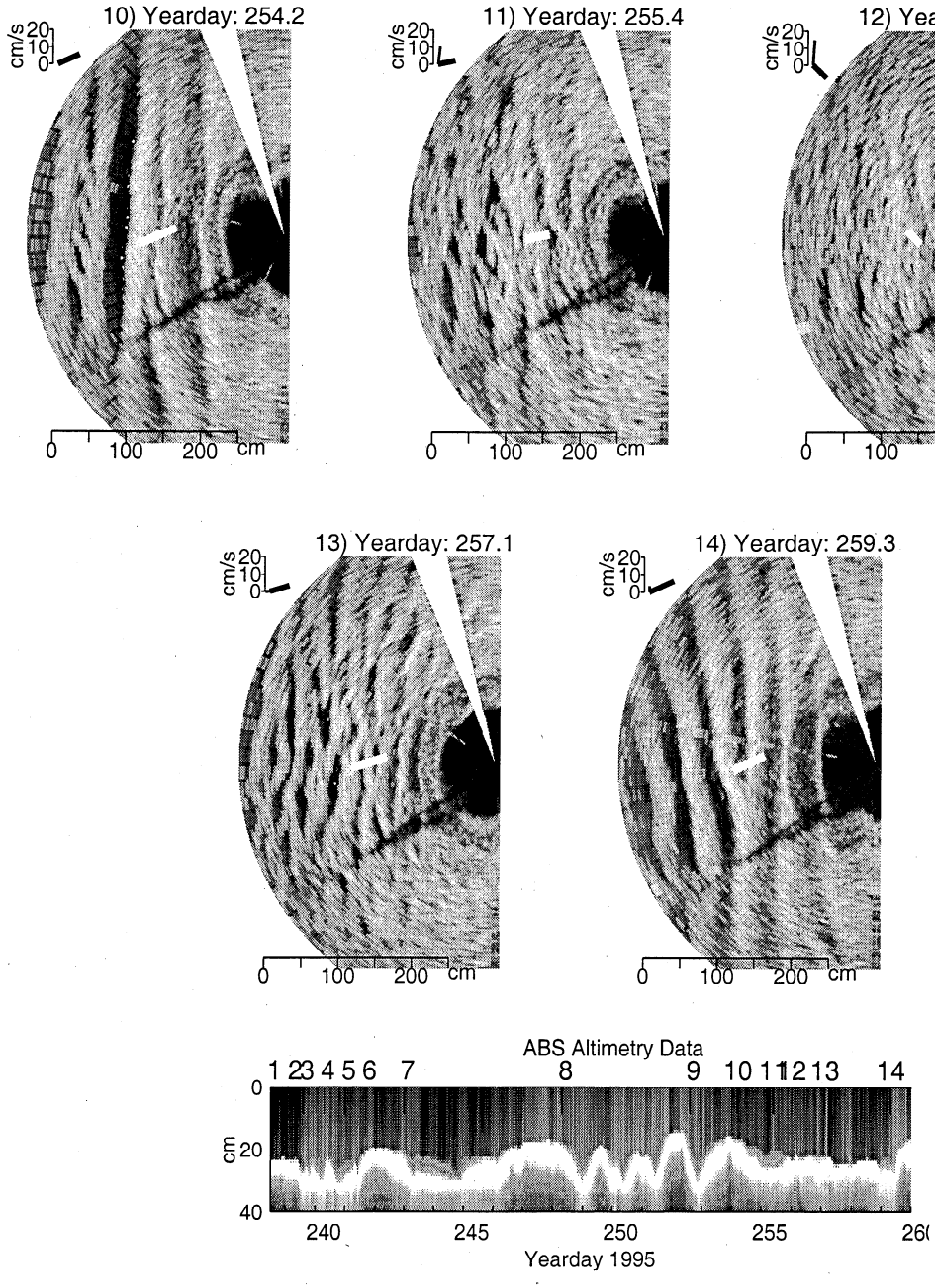

Figure 6. (continued)

θ_w^{sf} = 0.08 and θ_c^{sf} = 0.02 place these ripples in the wave ripple with superimposed, subordinate current ripples category of *Amos et al.* [1988], which is consistent with our observations. For most of our deployment, θ_c^{sf} is below 0.01 which according to *Amos et al.* [1988], is the region of wave-dominated ripples, as is consistent with our observations.

The period from yearday 244 to yearday 253 is marked by an increase in wave orbital diameter up to a maximum of 200 cm on yearday 253. The 2-D wave ripples increase in wavelength, up to a maximum of 100 cm (Image 9) in response to this forcing. On yearday 254 the waves have turned to a slightly down-coast direction again, and have decreased orbital diameter to about 80 cm. With this evolution of the wave forcing, instead of forming sinuous 3-D ripples as in Image 5 and turning to match the new wave direction, each of the large ripples begins to split along their crests into two ripples with half the wavelength (double the wavenumber) of the original ripples. These half-wavelength ripples are parallel to the original crests (Image 10). This can be best seen by examining the leftmost crest in Image 10. In between the crests of the split ripple a set of subordinate diagonal cross ripples that matches the new wave direction has begun to form. The primary difference in the evolution of wave forcing, and thus ripple pattern, between the period near yearday 241 (Image 5) and the period near yearday 254 (Image 10) is that in the first case the waves changed direction without substantially changing orbital diameter, while in the second the waves also changed orbital diameter as they changed direction.

The transitional pattern shown in Image 10 only lasts for several hours, because by yearday 255.4 (Image 11) the alongshore current speed becomes similar to the rms wave velocities. This has

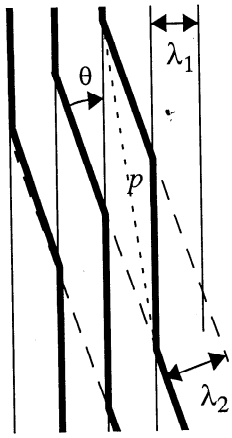

Figure 7. Along-crest variation length scale schematic. The dashed lines are the steady-state ripple patterns generated by waves before a directional shift through an angle θ. The thin solid lines are the steady state ripple pattern after the directional change. The thick lines are the transitional state (as seen in Figure 6, image 5) with along-crest oscillations of wavelength p.

the effect of disorganizing the nearly 2-D wave orbital ripples into a more isotropic 3-D pattern. By yearday 256 the current has become substantially stronger than the rms wave velocities and has almost completely eroded the wave orbital scale ripples. The poorly organized bedforms in Image 12 may be current ripples, but this image does not clearly show the current formed ripples that were visible in Image 7. Presumably, this period of ripple erosion is a period of large alongshore transport since the current is strong enough to flatten the 2-D wave ripples. In terms of relative wave versus current stress on yearday 256, $\theta_c^{sf} = 0.015$ and $\theta_w^{sf} = 0.025$. At this value of the wave Shields parameter the current Shields parameter must exceed 0.04 for current ripples to dominate, according to *Amos et al.* [1988]. This disorganized bedform pattern does not last long as the waves begin to form new 3-D wave ripples on yearday 257 (Image 13), which eventually organize into 2-D wave ripples as previously.

3.2. Temporal Evolution of Ripple Direction and Wavelength

From the rotary sidescan image data it is possible to measure time series of the geometric characteristics of the ripples such as wavelength and direction. A ripple direction estimate is found by manually locating end coordinates of a line normal to the ripple crests starting from the center of the image. The coordinate system is aligned such that a direction of 90° indicates a ripple with its crest running parallel to the average coastline orientation of 36°T. The projected distance along this line between several pairs of adjacent ripple crests is then used to estimate the ripple wavelength. If 3-D wave ripples are present, the wavelength is defined by the maximum separation between two adjacent crests. Enough pairs of points are chosen so that the standard deviation of the estimate is below 2 cm. In this procedure the first crest picked for a given image is the same as in the previous image so an estimate of ripple migration displacement between images can be found. Since the ripples only move a few centimeters per hour, as seen in the ABS altimetry record (Figure 6), there are no difficulties identifying the same ripple in consecutive images. When a ripple crest leaves the image, a new crest near the origin is tracked.

A high degree of correlation between ripple wavelength and scaled significant wave orbital diameter ($0.75d_{o,1/3}$) is generally evident in the time series shown in Figure 8. This indicates that the wavelength of these ripples does scale with wave orbital diameter. During periods when 3-D wave ripples are present the scaling factor appears to be smaller than 0.75.

Hysteresis effects (i.e. relic ripples) are visible at certain times during the deployment, as indicated in Figure 8. Most notably, at the beginning of the deployment 100-cm wavelength ripples were clearly visible in the sonar image from a storm which had occurred 1 week prior to the deployment. Near yeardays 242 and 253, delays of about one day are visible in ripples reacting to decreasing wave orbital diameter, before a step-like transition to the 2-D wave ripple state occurs. Step-like transitions are also noted during the onset of storms between 3-D wave ripples and 2-D wave ripples. However, once 2-D ripples have formed the ripples are

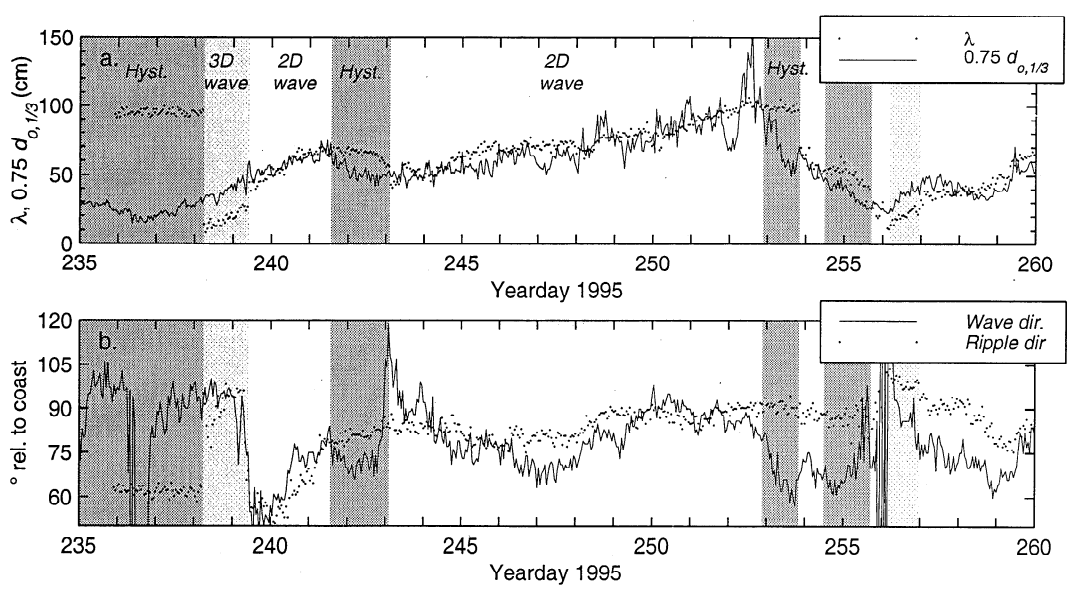

Figure 8. Temporal evolution of ripple features. (a) Ripple wavelength (λ) and scaled significant wave orbital diameter ($0.75d_{o,1/3}$). Wave ripple type (2-D wave, 3-D wave), and periods of hysteresis (Hyst.) or relic ripples are indicated by the shaded regions. (b) Ripple direction and dominant wave direction.

able to gradually adjust wavelength to match the increasing orbital diameter. This is somewhat consistent with the observation of *Boyd et al.* [1988] who noted "Storm arrival is accompanied by abrupt bed reorganization. In contrast as the storm moves away, a gradual step-like transition occurs through a characteristic sequence of reorganization and decay types." Here the abrupt reorganization is the change from 3-D to 2-D wave ripples, and Boyd et al.'s step-like transitions at the end of a storm are similar to the step-like transition from periods of hysteresis to the next ripple type.

The temporal evolution of ripple direction (Figure 8) also generally follows the dominant wave direction. Similar hysteresis effects to those seen in the wavelength time series are visible in the ripple direction time series. During the period from yearday 239 to 240, the ripple direction changes very closely match the wave directional changes. The largest discrepancy between ripple direction and wave direction occurs during the periods from yeardays 235 to 238 and 253 to 256. During the first period the ripples are relic ripples and are not in equilibrium with the hydrodynamic conditions. During the latter period large (λ=1 m) ripples are first being eroded by waves with a shorter orbital diameter and then by large currents. The ripple pattern during this period is characterized by large 2-D wave ripples matching the original direction and the subordinate wave ripples matching the new wave direction as described in section 2.1 (Figure 6, Image 10).

3.3. Empirical Models for Ripple Wavelength

Several authors have suggested linear relations between orbital diameter and ripple wavelength with similar scaling factors for wave ripples in a range of conditions. *Clifton and Dingler* [1984] summarized several data sets from both laboratory and field studies and suggested that ripple wavelength scales linearly with orbital diameter until wave orbital diameter/grain size (d/D) reaches a value of 2000. In the range of $2000<d/D<5000$ the ripples go through a transitional stage, which they called suborbital ripples. For values of $d/D>5000$, ripple wavelength scales directly with grain size and *Clifton and Dingler* [1984] suggested a scaling of $\lambda=400D$ to $600D$. *Wiberg and Harris* [1994] found a best fit with a scaling of $\lambda=535D$.

For the scaling parameter relating λ to $d_{o,1/3}$ *Inman* [1957] suggested a value of 1. *Komar* [1974] suggested a value of 0.8 as a better fit to the data. On the basis of only flume data, *Miller and Komar* [1980a] found a value of 0.65. *Miller and Komar* [1980b] also justified the use of d_o based on $H_{1/3}$, since they found that using $H_{1/3}$, as opposed to H_{rms}, gave better agreement to the relationship $\lambda=0.65d_o$ between field studies with irregular waves and laboratory studies with regular waves.

Wiberg and Harris [1994] classify ripple type based on the ratio of ripple height (η) to wave boundary layer thickness (δ_w). Since δ_w is roughly proportional to d_o, the classification ratio used is d_o/η. Limits of d_o/η = 20 and d_o/η = 100 are used to define the transitions from orbital to suborbital and suborbital to anorbital scale ripples. Classifying our data set based on observed η and $d_{o,1/3}$ results in all the ripples being classified as orbital scale ripples (see section 3.6. for a discussion of observed ripple heights). For orbital scale ripples the predicted ratios of η_{orb}/λ_{orb} =.17 and λ_{orb}/d_o=.62 are both constant and thus η_{orb}/d_o=0.1 is also constant. Therefore d_o/η_{orb} cannot be used to predict a transition to suborbital or anorbital ripples. *Wiberg and Harris* [1994] resolved this problem by using the ratio of orbital diameter to anorbital ripple height (d_o/η_{ano}) to define the transition. An empirical relationship was found to relate anorbital steepness to the ratio d/η_{ano}:

$$\frac{\eta_{ano}}{\lambda} = \exp\left[-0.095\left(\ln\frac{d}{\eta_{ano}}\right)^2 + 0.442\ln\left(\frac{d}{\eta_{ano}}\right) - 2.28\right] \quad (11)$$

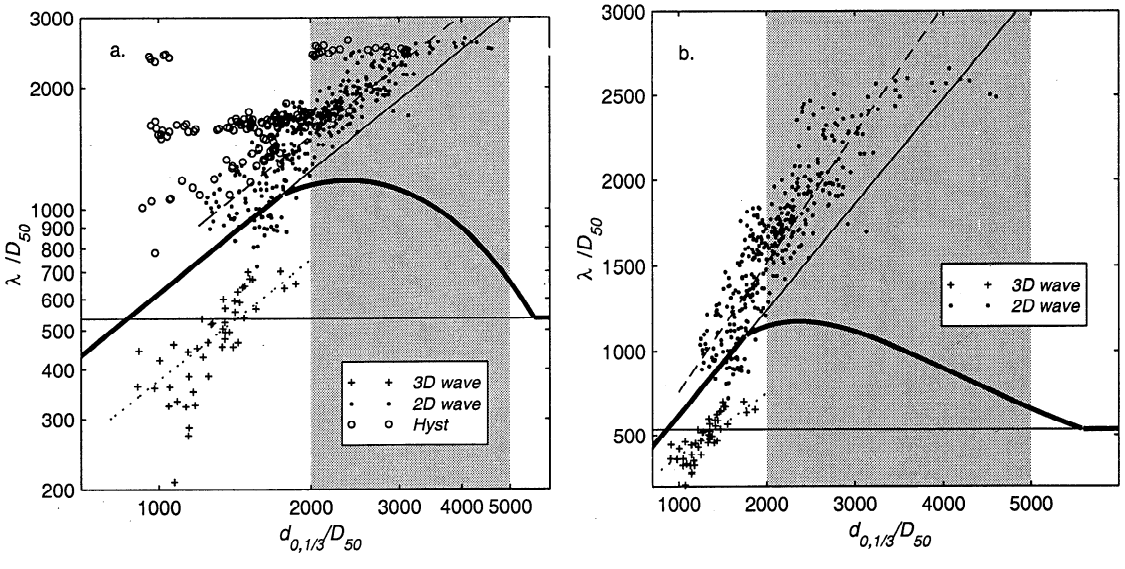

Figure 9. (a) Ripple wavelength (λ) as a function of wave orbital diameter ($d_{o,1/3}$), with both quantities scaled by measured median grain size D_{50}=400 μm. Points represented by open circles are during times of hysteresis (relic ripples) as determined from the time series. (b) Same as Figure 9a, but hysteresis points not displayed and linear axis scaling. Points represented by crosses are 3-D wave ripples with a scaling of $\lambda=0.38d_{o,1/3}$ shown as a dotted line. Points plotted as dots are 2-D wave ripples with a best fit line of $\lambda=0.76d_{o,1/3}$ shown as dashed line. The thick solid line is the *Wiberg and Harris* [1994] empirical model with the orbital scaling of $\lambda=.62d_o$ and anorbital scaling of $\lambda=535D$ continued beyond the transitional (shaded) region as thin lines.

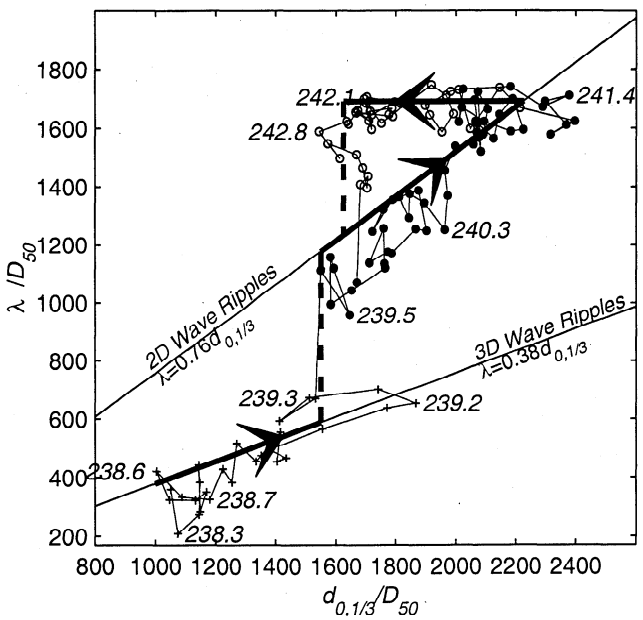

Figure 10. Temporal evolution of ripple wavelength as a function of wave orbital diameter with both quantities normalized by median grain size (D_{50}=40 0μm). The 2-D (dots), and 3-D (crosses) wave ripples, and relic ripples (open circles) data points are connected by lines in the order of occurrence. The time of selected points is shown. The thick arrows are a conceptual model for the temporal evolution. The diagonal upward thick black lines are the trajectories along the orbital ripple scaling relations of $\lambda=0.38d_{o,1/3}$ and $\lambda=0.76d_{o,1/3}$. The horizontal line with an arrow pointed to the left is the hysteresis path.

Since $\lambda_{ano}=535D$ and d_o/η_{ano} = 20 and d_o/η_{ano} = 100 define the transitions, (11) can be used to find the transitional points of d_o/D=1754 for orbital to suborbital and d_o/D=5587 for suborbital to anorbital. These values are fairly close to *Clifton and Dingler*'s [1984] transitions at d/D=2000 and 5000.

To examine where our data falls in the context of this type of model, the ripple wavelength (λ) normalized by measured median grain diameter (D_{50}=400 μm) is plotted against significant wave orbital diameter normalized by median grain diameter ($d_{o,1/3}/D_{50}$) in Figure 9a. The data points during periods of hysteresis are clustered along horizontal bands of constant ripple wavelength at λ/D_{50}=1700 and 2600. The hysteresis point located in the upper left corner of Figure 9 are also characterized by $\theta_w^{sf} < \theta_{crit}^{sf}$, as defined in section 1.3. The remaining data points fall into two clusters depending on ripple type. The 2-D wave ripple data points are well fit by a linear model of $\lambda=0.76d_{o,1/3}$ and have a correlation coefficient of R^2=0.86. The 3-D wave ripple data points are also well fit by a linear model with a different slope of $\lambda=0.38d_{o,1/3}$ and have a correlation coefficient of R^2=0.80. A slightly better fit to the 3-D wave ripple data points can be achieved if a linear model with an offset is used: $\lambda=0.46d_{o,1/3}$-5.0. While negative wavelengths are impossible, it is not implausible that the curves do not need to be extrapolated to pass through the λ=0, d_o=0 point because of thresholding effects.

3.4. Temporal Evolution in λ/D, d_o/D Space

As an alternate method of examining effects such as hysteresis, one can examine the temporal evolution of the relation between λ/D_{50} and $d_{o,1/3}/D_{50}$. The evolution of ripple wavelength over one storm event from yearday 238.2 to yearday 243.15 is shown in Figure 10. The ripples start as 3-D wave ripples and increase wavelength in response to increasing wave orbital diameter roughly along the 3-D wave ripple orbital relation line of $\lambda=0.38d_{o,1/3}$. By yearday 239.3 the ripples become organized into 2-D wave ripple and increase wavelength along the 2-D wave ripple orbital relation line of $\lambda=0.76d_{o,1/3}$. By yearday 241.5 the ripples are close to their maximum wavelength, for this particular storm, of approximately 68 cm (λ/D_{50}=1700) due to waves with $d_{o,1/3}$=88 cm ($d_{o,1/3}/D_{50}$=2200). During the next day, a hysteresis period occurs as the wave orbital diameter diminishes and the ripples maintain a constant wavelength. By yearday 243 a strong current event combined with waves with $d_{o,1/3}/D_{50}$=1700 reduces the ripple wavelength by a factor of 2/3. While the ripples do not exactly follow this type of three step triangular trajectory in λ/D_{50}, $d_{o,1/3}/D_{50}$ space for every storm, it is a fairly typical sequence of events. The hysteresis (relic ripples), in particular, where the ripples maintain constant wavelength for some period while the wave orbital diameters are diminishing is seen at the end of all the storm events in this data set.

3.5. Maximum Ripple Wavelength and Transition to Suborbital Scaling

The data show a maximum ripple wavelength of about 100 cm (λ/D_{50}=2500) despite the fact that the wave orbital diameter exceeds 130 cm ($d_{o,1/3}/D_{50}$=3250) for 10 hours near yearday 253 (Figure 8). There are more than 10 hourly sampled ripple wavelength points in Figure 8 and Figure 9 at the maximum wavelength of 100 cm due to hysteresis effects. With the waves only exceeding the linear relation for a short time it is not clear that this is indeed the maximum wavelength ripple that will form at LEO-15 and that the data points with λ=100 cm for $d_{o,1/3}$ greater than 130 cm are in the transitional region. If the waves were to get significantly longer than 130 cm for extended periods of time and ripple wavelengths remained at 100 cm, this would be a clear indication of a transitional stage with a maximum wavelength of 100 cm. The probability of seeing such large waves at LEO-15 for an extended time is discussed in section 6.

According to the models, the transition to suborbital scaling should occur just after the orbital diameter exceeds the diameter which would cause the maximum predicted ripple wavelength. If we are indeed seeing a transition to suborbital ripples near an orbital diameter of $d_{o,1/3}$=130 cm ($d_{o,1/3}/D_{50}$=3250), scaling the data by the median grain size of D_{50}=400 μm would indicate a transition in the data at about $d_{o,1/3}/D_{50}$=3250 as opposed to $d_{o,1/3}/D_{50}$=2000, as predicted by the *Wiberg and Harris* [1994] model (Figure 9a). For a D_{50}=400 μm grain size scaling, the maximum wavelength predicted by the model is 47 cm (λ/D_{50}=1175). This is much smaller than the maximum observed wavelength of 100 cm. However, if a larger grain size scaling of D_{85}=800 μm is used, the transition does occur near d/D=2000 and the data, including the maximum observed wavelength of 1 m, is well fit by the *Wiberg and Harris* [1994] model, as seen in Figure 9b. This larger grain size of D_{85}=800 μm is approximately one standard deviation above the median grain size. For our data, scaling the model by the observed median grain size D_{50}=400 μm results in

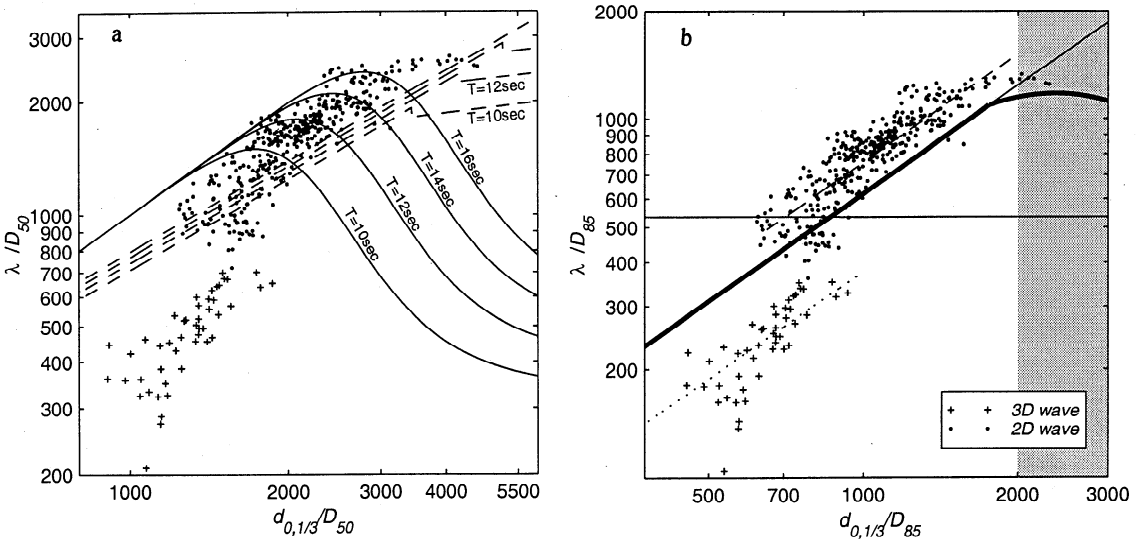

Figure 11. (a) Ripple wavelength as a function of significant wave orbital diameter with both quantities normalized by measured median grain size D_{50}=400 μm. The *Nielsen* [1981] model is shown as the solid lines with wave periods varying from 10-16 s. The *Grant and Madsen* [1982] model, also with periods from 10-16 s, is shown as the dashed lines. (b) Same as Figure 9a (the *Wiberg and Harris* [1994] model), but normalized by D_{85}=800 μm. The best fits to the 3-D and 2-D wave ripple data are shown as the dotted and dashed line, respectively.

an incorrect prediction of a transition to suborbital ripples as well as an under-prediction of the maximum ripple wavelength.

The largest wave orbital scale ripples that were included in the references to field data sets that *Wiberg and Harris* [1994] used to construct their empirical model were the λ=100 cm ripples observed in D_{50}=500 μm sand by *Inman* [1957], which are also somewhat larger than the maximum predicted ripple wavelength of λ=68 cm for D_{50}=500 μm sand.

Miller and Komar [1980a] suggested an empirical formula for maximum ripple wavelength based largely on laboratory studies of

$$\lambda = 0.0027 D^{1.68}. \tag{12}$$

With D_{50}=400 μm sediment this formula predicts a maximum ripple wavelength of 65 cm, which is also considerably smaller than the 100 cm wavelengths observed at LEO-15.

While *Clifton and Dingler* [1984] and *Wiberg and Harris* [1994] suggest that anorbital ripple wavelength scales with grain size alone, and thus the transitions can be defined in terms of d_o/D, other authors describe anorbital ripple wavelengths as functions related to bottom stress. Based on field data by *Inman* [1957], *Dingler* [1974] and *Miller and Komar* [1980b], *Nielsen* [1981] found λ/A as a function of mobility number (ψ):

$$\frac{\lambda}{A} = \exp\left(\frac{693 - 0.37\ln^8\psi}{1000 + 0.75\ln^7\psi}\right) \tag{13}$$

Mobility number is a measure of bottom stress forces ($\propto$ velocity^2) acting to move the sediment relative to gravitational forces stabilizing the sediment and is defined as

$$\psi = \frac{(A\omega)^2}{(s-1)gD} \tag{14}$$

where $A=d_o/2$ is the wave orbital excursion amplitude, ω is the wave frequency, g is gravity, and $s=\rho_s/\rho_w$ is the ratio of sediment density to water density. With this type of model the transition to the anorbital type of scaling depends not only on grain size and wave orbital diameter, but also on wave period. At longer wave periods the transition to anorbital scale ripples occurs at larger orbital diameters, as shown in Figure 11. This also allows the model to predict larger maximum wavelength ripples at longer wave periods before a transition occurs.

Our data show a maximum wavelength of 100 cm near yearday 253. During this storm, the wave periods reached 14-16 s. With wave periods of 16 s *Nielsen*'s [1981] model predicts a maximum wavelength of 96 cm (λ/D_{50}=2400), consistent with our observed maximum wavelength of 100 cm.

Although the *Grant and Madsen* [1982] model does not explicitly contain a linear relation between orbital diameter and ripple wavelength, the equations for η/A and η/λ define a nearly linear relation in their "equilibrium range." The slight variations from a linear relation are seen by the varying position, as a function of wave period, of the dashed lines in Figure 11a. This model defines a transition to a regime of lower ripple steepness at a "break-off" skin friction wave Shields parameter value. Since the Shields parameter is dependent on both wave period and velocity, this model, like the *Nielsen* [1981] model, defines a transition that does not only depend on d_o/D. The *Grant and Madsen* [1982] model predicts the maximum observed ripple wavelength with a wave period of approximately 13 s.

The physical justification for the larger maximum wavelength ripples at longer wave periods could be that with the lower velocities associated with longer-period waves with the same bottom orbital diameter as shorter-period waves with higher velocities, the sediment transport is dominated by bedload rather than suspended transport. Presumably, the bedload mode is more conducive to orbital scale ripples, while fully suspended transport favors anorbital ripples or sheet flow conditions. This may be due to the fact that as suspended load more sediment is able to by-pass the ripple trough. Bedload-forced formation of orbital scale ripples may also

be related to the required scaling by a larger grain size to make the LEO-15 data agree with the empirical models that do not take wave period into account, since the larger grains are more likely to be transported as bedload rather than suspended load.

3.6. Ripple Height

The second important parameter that is used to describe the geometry of nearly 2-D wave ripples is ripple height (η). The instruments deployed on the LEO-15 tripod allow two different methods of estimating the temporal evolution of ripple height.

The bottom return from the ABS data can be used to estimate the distance to the local seafloor from the sonar head (Figure 2 and Figure 3). As a ripple migrates past the beam, a height can be determined from the difference between crest and trough elevation. This gives a discrete time series with each height estimate generated at the time between the passage of a crest and trough. The 30° beam width of the ABS gives a footprint of 50 cm, as defined by the half power points. This could produce an error of a few centimeters in estimating the depth of the trough with large ripples and completely averages out the height variations associated with ripples of wavelength much less than 50 cm. Data from a second acoustic backscattering system with a very narrow beam (2-cm footprint) that was operational until yearday 243 gives a similar height estimate to the ABS system since most of the ripples observed at LEO-15 had wavelengths greater than 50 cm.

The second height estimate is generated from the intersection of the SSS beam pattern with the seafloor. The first bottom return in the SSS data is generated when the lower edge of the beam pattern, which is angled down at 45°, hits the bottom. This appears in the sector scanner images as the edge between the black region in the center of the image and the grey area where the sound beam is hitting the bottom (Figure 3). The variations in distance of this edge from the center of the image are clearly visible as the beam rotates around to point at the ripple trough and then the ripple crest. This distance is represented by the line AB in Figure 12. If the variations in the length of line AB as the sector scanner rotates around are multiplied by a factor of cos(45°), a series of elevation estimates (h-ζ) can be generated around the r~1 m radius circle where the SSS beampattern intersects the bottom. Here ζ is defined as the local surface elevation above the ripple trough. The standard deviation of the h-ζ estimates is then multiplied by a factor of $2\sqrt{2}$ to give an estimate of ripple height (η). This is based on assuming a sinusiodal ripple profile, since for a sine wave the height is equal to $2\sqrt{2}$ times the elevation standard deviation (for a triangular ripple profile assumption, the factor would be $2\sqrt{3}$). However, assuming a sinusiodal profile gives reasonable agreement with the ABS estimate, thus $2\sqrt{2}$ is used.

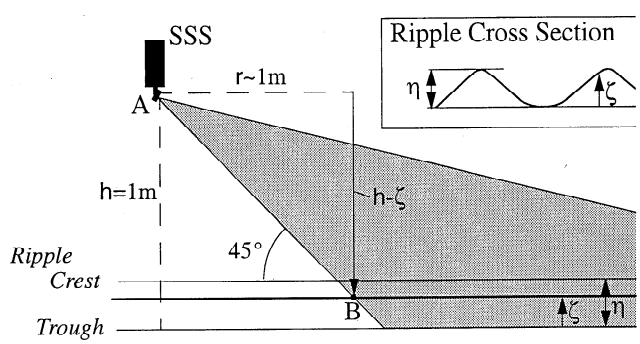

Figure 12. An estimate of ripple height can be calculated from each sector scan image by examining changes in the distance AB from the transducer head (A) to the point of intersection of the lower edge of the beam pattern with the ripple surface (B). The distance AB changes as the transducer rotates to aim the beam at different locations on the ripple surface.

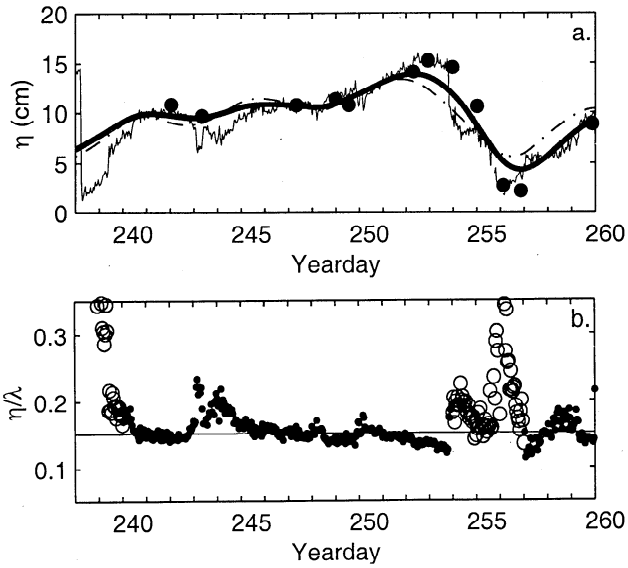

Figure 13. Evolution of ripple heights. (a) Ripple heights (dots are the ABS altimeter estimates, dash-dot line is the SSS sidelobe estimate, and thick line is the average of the two estimates) and ripple wavelength scaled by 0.15 (thin solid line) as a function of time. (b) Ripple steepness (η/λ) as a function of time. The open circle points are not reliable as described in the text, and are not included in the calculation of the mean (thin line, at η/λ=0.15).

While the SSS ripple height estimate generates hourly estimates of ripple height as opposed to the ABS estimate which depends on migration speed, the SSS estimate has an error depending on whether the SSS is located over a ripple trough or crest. The SSS estimate is low-pass filtered with a smoothing filter that has a timescale of the longest ripple migration crest-to-crest time. The ABS estimates are interpolated with an interpolator that also has a similar timescale. The ABS and the SSS height estimates are averaged to give a single time series for calculation of ripple steepness, as shown in Figure 13.

The periods of high apparent steepness near yeardays 239 and 255 are probably not very significant since the ripple height estimate has the most error when the ripples are small and migration rates are low. Given the errors inherent in both methods of estimating ripple heights, the mean steepness of η/λ=.15 for the entire deployment is the most confident statement that can be made about ripple steepness. The periods of small ripples and high steepness denoted by open circle points in Figure 13b were not included in this mean. This quantity agrees reasonably well with average steepness for wave orbital ripples of η/λ=0.17 reported by *Wiberg and Harris* [1994], η/λ=0.18 reported by *Nielsen* [1981], and η/λ=0.16 reported by *Grant and Madsen* [1982]. Just as a transition to anorbital ripple scaling was not evident in the wave-

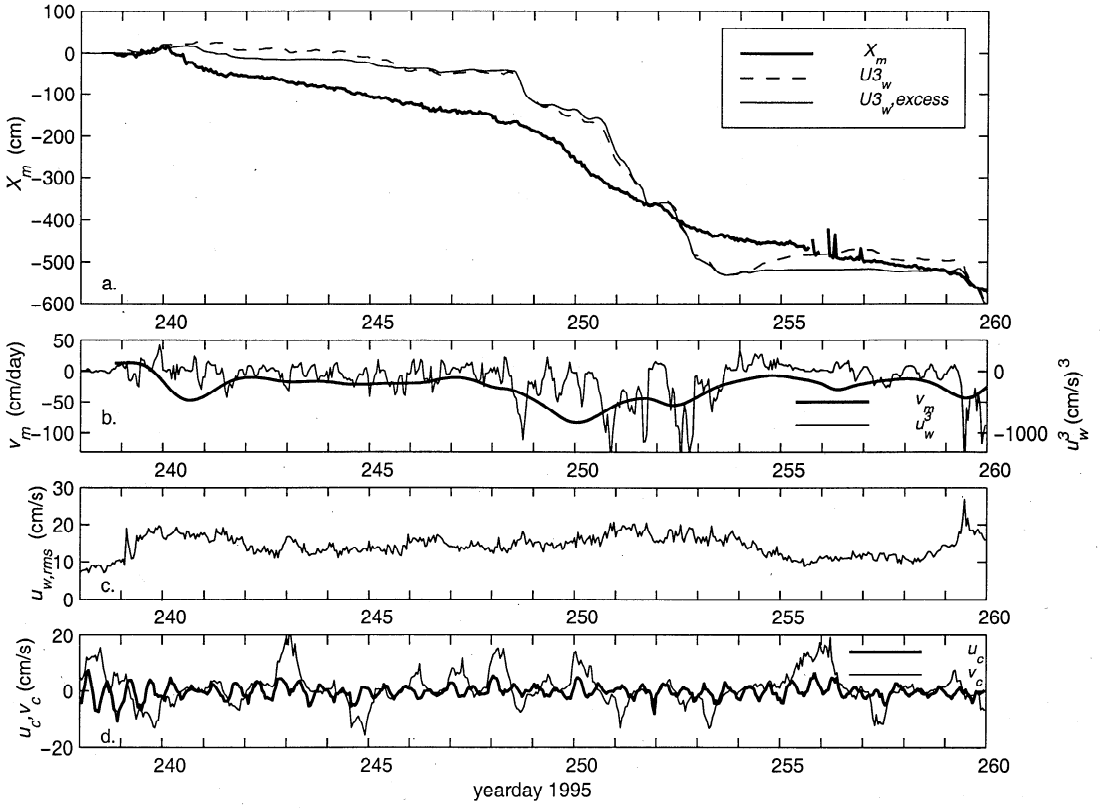

Figure 14. Ripple migration as related to wave and current parameters. (a) Ripple crest displacement, X_m (thick line), $U3_w$ (thin dashed line) and $U3_{w,\text{excess}}$ (thin line). (b) Ripple crest velocity v_m (thick line, left y-axis), and $\overline{u_w^3}$ (thin line, right y-axis.) (c) Root mean square wave velocity ($U_{\text{w,rms}}$) (d) Alongshore (v_c, thin line) and cross-shore (u_c, thick line) current velocities from BASS burst averages 44 cm above the seafloor. The cross-shore current is dominated by the semi-diurnal tide, is relatively weak, and thus transports little sediment compared to waves.

length data, no evidence for a transition to a decreased steepness regime is evident in the steepness data.

4. Ripple Migration

Although the geometrical properties of wave ripples are important for their effect on the boundary layer hydrodynamics, and thus sediment transport, perhaps one of the important mechanisms for cross-shore material transport is the migration of ripples. Ripple migration displacement is found by tracking the coordinates of a particular ripple crest as discussed in section 2.1. Displacement is only measured in a direction normal to the ripple crests. Since the ripples are generally aligned with crests running nearly parallel to the coast, the direction of migration is referred to as simply on-offshore, even though there may be some small alongshore component. The coordinate system used in this paper has the positive directions oriented offshore and up-coast.

The cumulative ripple migration displacement (X_m) found by summing the hourly interimage displacements from time zero (yearday 238) to the time indicated on the x-axis is shown in Figure 14a. This figure also shows the rate of migration (v_m) computed from the temporal derivative of the smoothed cumulative migration displacement. The direction of migration is seen to be consistently onshore with the only apparent exception occurring near yearday 240. This is a period during which the ripple direction is turning rapidly (Figure 8b), and thus a particular section of ripple may be moving offshore as the ripple pattern evolves.

The total onshore migration of the ripples is 600 cm over a period of 25 days, thus giving a average onshore migration rate of 24 cm/day. Peak rates of 80 cm/day in the onshore direction are seen around yearday 250 when the ripples have the longest wavelengths observed throughout the deployment (Figure 14b).

The ripple migration rate is seen to be greatest when the wave energy is highest (Figure 14c) and does not appear to be related at all to either component of current velocity (Figure 14d). In particular, ripple migration is in the across-shore direction (aligned with the waves) and currents in the across-shore direction are dominated by the weak (5 cm/s) semidiurnal tides. This would indicate that current is not a forcing mechanism for ripple migration. In addition, purely linear monochromatic wave motion with no superimposed current would result in equal velocities in either direction and thus no transport. Wave nonlinearity as waves enter shallow water results in asymmetric velocity distributions about the mean velocity with larger onshore velocities for shorter periods and longer periods of weaker offshore velocities. This can clearly result in a net transport of sand and thus possibly force ripple migration, particularly if there exists a threshold for sand movement that is exceeded more often by the onshore velocities.

To determine if wave nonlinearity is a direct forcing mechanism for ripple migration, one could examine wave skewness (s) calculated from the BASS sensor 44 cm above the bed.

$$s = \frac{\overline{u_w(t)^3}}{u^3_{w,\,rms}} \tag{15}$$

Skewness, however, weights large velocity waves equally to small velocity waves because of the $u^3_{w,\,\mathrm{rms}}$ in the denominator. Physically, waves with larger velocities would be expected to mobilize greater amounts of sand so a better forcing mechanism may be the burst averaged $u_w{}^3$ shown in Figure 14b.

$$\overline{u_w^3} = s u^3_{w,\,\mathrm{rms}} \tag{16}$$

In the coordinate system with negative u directed onshore, negative $\overline{u_w^3}$ indicates larger onshore velocities. The $\overline{u_w^3}$ record shows several negative peaks near yearday 250 and 259 consistent with a period of fast ripple migration. The $\overline{u_w^3}$ time series shows a high degree of variability at the semidiurnal tidal frequency, especially near periods of rapid migration, such as near yearday 250. The tidal variability in $\overline{u_w^3}$ is most likely forced by the tidal flows across the ridge, as out going (positive) tidal currents can cause an increase in wave steepness which in turn increases (negative) $\overline{u_w^3}$. This is evident in Figure 14b just after yearday 250. If tidal variability exists in the ripple migration velocity record, it is not seen since a substantial amount of smoothing is required in taking the derivative of the measured displacement record (X_m) to get migration velocity (v_m). The smoothing is required because of high-frequency noise in X_m.

Since X_m is the actual measured ripple displacement, it is more appropriate to look at a forcing function that can be directly compared to X_m, such as the cumulative time integral of the wave forcing. In Figure 14a the cumulative integral of $\overline{u_w^3}$ is plotted with a single scaling constant to fit the ripple migration data.

$$U3_w(t) = \int_o^t \overline{u_w^3(t')}\,dt' \tag{17}$$

While the general shape of $U3_w$ time series matches the ripple displacement fairly well, $U3_w$ would indicate greater migration during the most extreme event near yearday 250 and less migration during the other times (capital variables are used to denote cumulative quantities). A second similar function was also investigated.

$$U3_{w,\,\mathrm{excess}}(t) = \int_o^t \overline{(u_{w,\,\mathrm{excess}})^2 u_w}\,dt'$$

$$u_{w,\,\mathrm{excess}} = \begin{cases} |u_w| - u_{\mathrm{crit}} & |u_w| > u_{\mathrm{crit}} \\ 0 & |u_w| < u_{\mathrm{crit}} \end{cases} \tag{18}$$

The critical velocity (u_{crit}) for initiation of sediment motion of approximately 25 cm/s was found by using the methods discussed in section 2.2. This function should emphasize the larger waves more than $U3_w$, since waves with velocities below u_{crit} are not included in the mean. However, both $U3_w$ and $U3_{w,\mathrm{excess}}$ give fairly similar results. Both of these proposed forcing functions are attempting to relate ripple migration to an integrated wave statistic. This does not account for the possibility that larger ripples may require greater amounts of wave motion to force ripple migration at the same rate as smaller ripples. This concept will be discussed further in the next section.

4.1. Sediment Transport Due to Ripple Migration and Suspended Sediment Transport

To further investigate a possible forcing mechanism for ripple migration, suspended sand transport itself can be examined. Since the observation system measures both water velocity and vertical profiles of sand concentration, instantaneous Eulerian transport rate calculations can be performed by multiplying these two quantities together, assuming that sediment moves at the water velocity.

$$\vec{q}(z) = \vec{u}(z)C(z)\,. \tag{19}$$

The sand concentration profile is measured from 80 cm above the bed to within a few centimeters of the bed, where the bottom return contaminates the acoustic backscattering measurement of suspended sediment.

Suspended sediment transport rates were calculated with both the mean current velocities ($\vec{u_c}(z)$) and wave velocities (u_w). The depth dependence of the steady current was calculated by fitting a log profile to the BASS current meter vertical array. It was found that the net sediment transport due to the mean currents was a factor of 5 less than the transport due to wave velocities [*Traykovski*, Wave Forced Suspended Sediment Transport at the Sandy Inner Continental Shelf LEO-15 Site, submitted to *J. Geophys. Res*, 1998]. The net suspended sediment transport due to the current is also mostly in the alongshore direction with only a small component in the across-shore direction. Since the wave velocity contribution to sediment transport is much larger than the current component and the ripples migrate in the across-shore direction of the wave propagation, only the wave component of transport is considered as a possible forcing function for ripple migration.

For u_w the velocity is assumed to be constant with depth over the lower 80 cm of the water column. Since most of the longer-period waves at LEO-15 are shallow water waves, this should be valid outside of the thin wave boundary layer. By examining wave velocities along the BASS vertical array it was confirmed that wave velocities were relatively constant with depth over the lower portion of the array. The height of the wave boundary layer over large orbital scale ripples is not well-defined for wave orbital scale ripples since wave boundary layer models predict a boundary layer thickness smaller than the ripple height. In fact, the *Wiberg and Harris* [1994] wave ripple model defines wave orbital ripples as having heights larger than the wave boundary layer. The boundary layer that does exist is probably a transient boundary layer that forms on the upstream face of ripple before the flow detaches at the ripple crest. The amount of suspended sediment transported by the wave velocities in a burst is calculated by

$$m_{\mathrm{suspended},\,w}(z) = \sum_0^{T_b} C(z)u_w\Delta t \tag{20}$$

Here Δt is the temporal burst sampling interval of 0.5 s and T_b is the burst length of 240 s from the ABS sampling schedule. The units of m_b are g/cm^2, and m is related to the average sediment transport rate by

$$\bar{q} = \frac{1}{T_b} m \tag{21}$$

Figure 15a shows the cumulative sum of depth-integrated, burst-integrated wave-induced transport

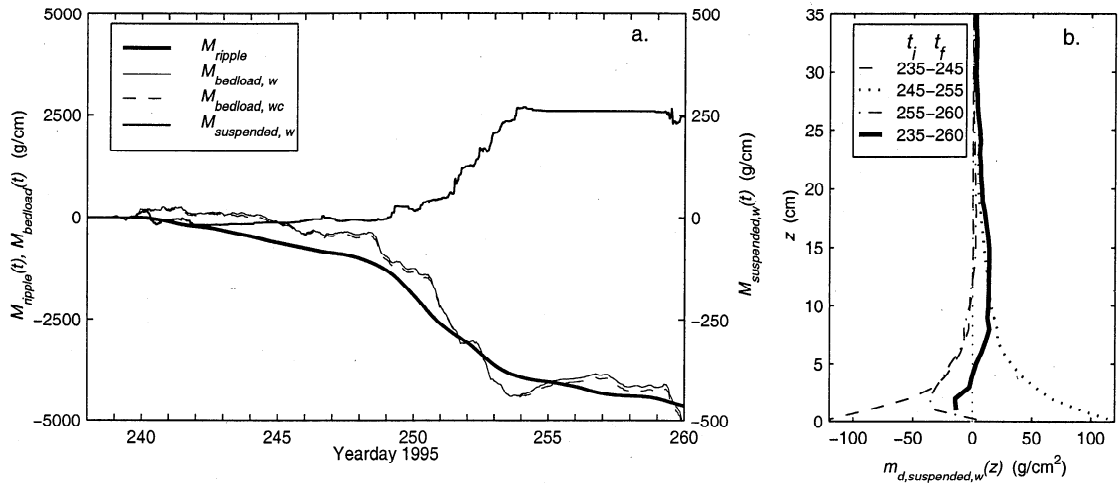

Figure 15. Suspended sand transport and Ripple sand transport. a) Temporal evolution of cumulative net depth-integrated suspended transport ($M_{\text{suspended},w}$). The scale for $M_{\text{suspended},w}$ is on the right y-axis. M_{ripple} is the sand transport associated with ripple migration based on the assumption that ripples transport their entire volume of sand. The scale for M_{ripple} is on the left y-axis. Also shown are the bedload model forced with wave stresses ($M_{\text{bedload},w}$, left y-axis) calculated by the instantaneous wave velocities ($u_w(t)$) and forced with combined wave-current stresses ($M_{\text{bedload},wc}$, left y-axis) (b) Depth dependent transport $m_{c,\text{wave}}$ for periods yearday 235 to 245 (dashed line), 245 to 255 (dotted line), 255 to 260 (dash-dotted line), and 238 to 260 (thick line). Negative transports are onshore.

$$M_{\text{suspended},w}(t) = \sum_0^t \sum_{z=0}^{z_{\max}} m_{\text{suspended},w}(z,t)\frac{\Delta T_b}{T_b} \qquad (22)$$

$$z = z_{\min} - z_t$$

The units of $M_{\text{suspended},w}$ are g/cm width. The time t is the time from the beginning of the deployment. The factor of $(\Delta T_b/T_b)$ is the ratio of the burst length (T_b) to the inter-burst time (ΔT_b) of 30 min. This accounts for the fact that burst sampling only occurs for a fraction of the total time and assumes stationary statistics for estimating the total transport, which may not be fully valid since the suspension process depends strongly on the tails of the wave velocity distribution. The depth variable z is defined as the distance from the instantaneous local bottom, and z_t is the distance from sonar transducer. The change of variables from z to z_t in (22) places the temporal averaging across depth bins into a coordinate system relative to the instantaneous local bottom elevation. The lower limit of depth integration, $z_{\min}$, is set at 6 cm above the maximum bottom return to avoid calculating transport with range cells that are contaminated by the bottom return. The upper limit of integration, $z_{\max}$, is set 80 cm above $z_{\min}$ since the wave-induced transport is generally close to zero at this height.

As a first-order estimate of the error in the suspended sediment transport calculation caused by integrating only to within 6 cm of the bottom, the calculations in (20) and (22) were repeated with the depth-averaged sediment concentration in the bottom 3 cm (6-9 cm above bottom) extrapolated down an additional 5 cm. This had the effect of increasing $M_{\text{suspended},w}$ from 260 g/cm to 360 g/cm. While this is a substantial difference, it is of the same order as the potential factor of 2 error from the ABS concentration estimate.

To examine the depth dependence of this process, the time-integrated net depth dependent mass transport can be calculated by

$$m_{d,\text{ suspended},w}(t,z) = \sum_0^t m_{\text{suspended},w}(z,t)\frac{\Delta T_b}{T_b} \qquad (23)$$

This quantity is plotted for the time intervals yearday 235 to 245, 245 to 255, 255 to 260, and for the whole deployment in Figure 15b. These three periods were chosen since there is offshore transport in the first, onshore in the second and offshore again in the third. By examining the thick line in Figure 15b it is evident that for the entire deployment the transport is directed offshore above z=7 cm and onshore below z=5 cm. The positive y direction in Figure 15 is offshore, thus the total cumulative wave-induced transport ($M_{\text{suspended},w}$) over the entire deployment is directed offshore. During the period from yearday 250 to 254 where onshore ripple migration displacement is greatest, the wave-induced suspended transport is also large but in the offshore direction. Over the entire period yearday 238 to 260 the amount of suspended transport is a factor of 20 less than the transport associated with ripple migration (M_{ripple}), as seen in Figure 15a.

The total mass of sediment per unit cm width associated with the ripples that migrated past the SSS system at any time t can be estimated as

$$M_{\text{ripple}}(t) = \int_0^t \rho_s(1-\varepsilon)\zeta V_m dt \qquad (24)$$

where ρ_s is the sediment density in g/cm^3, ε is the porosity (ε=.35) [*Sleath*, 1984], ζ is the instantaneous ripple elevation, and V_m is the rate of migration. M_{ripple} is plotted in Figure 15a.

Equation (24) can be derived by examining the continuity equation for sediment mass (Figure 16), [*Engeleund and Fredsoe*, 1982]

$$\frac{\partial q}{\partial x} = \rho_s(1-\varepsilon)\frac{\partial}{\partial t}\zeta \qquad (25)$$

If the bedforms are assumed to migrate with velocity V_m and maintain constant shape (i.e., $\zeta = F(x - V_m t)$) then

$$\rho_s(1-\varepsilon)\frac{\partial}{\partial t}\zeta = -\rho_s(1-\varepsilon)V_m\frac{\partial}{\partial x}\zeta \qquad (26)$$

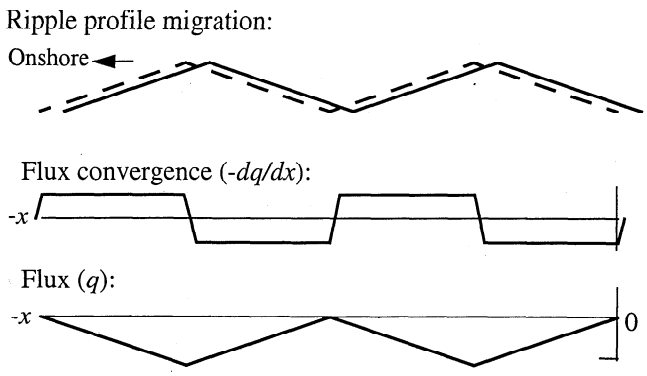

Figure 16. A simple conceptual model for relating bedload transport to ripple migration. The migration of the ripple profile over half a wave cycle is related to the temporally integrated flux convergence over the half wave cycle. The diagram is shown for the onshore half cycle of wave motion.

and thus

$$q = \rho_s(1-\varepsilon)V_m\zeta + q_0 \tag{27}$$

Here q_0 is an arbitrary constant of integration which is set to zero on basis of the assumption that the ripples transport their entire volume of sand with them. This is not generally the case. In unidirectional flows, bedforms can migrate the opposite direction to the net transport. For low shear stresses, where most of transport occurs as bedload, q_0 is often assumed to be zero in unidirectional flows [*Fredsoe and Deigaard,* 1992]. If there is no exchange of sediment from one ripple to the next, this is a valid assumption. For wave orbital scale ripples the bedload transport is limited to a distance equal to or less than one ripple wavelength, while suspended load may be able to travel a slightly longer distance in each wave cycle. While the ABS instrument is unable to resolve the thin layer of sediment transport with a few centimeters of the ripple surface, it is unlikely that sediment is transported from one ripple to the next in this thin layer. Reasons for this include the high velocity shear within the wave boundary layer and the generation of eddies in the lee of each ripple that limit the transport distance. Outside of this thin layer the ABS does not observe a sufficient amount of suspended sediment transport to make the constant of integration (q_0) substantially different from zero. From qualitative laboratory observations it is evident that with wave orbital ripples most of the sand exchange from one face of a ripple to another occurs over the crest of the ripple and not the trough [*Bagnold,* 1946]. With these constraints the sand transport associated with the ripple migration should approximately equal the volume of sand contained in the ripples times the migration rate.

Unfortunately, the ABS system is unable to observe the thin layer of bedload or near-bottom suspended transport that is responsible for forcing the ripple migration, and the ripple transport is in the opposite direction and an order of magnitude larger than the wave-induced sand transport 6 to 80 cm above the bottom that the ABS does observe. Thus it is hypothesized that bedload or near-bottom suspended transport that is not well observed by the ABS and current meter system is the dominant form of cross-shelf transport for the medium to coarse grained sediments that occur on the ridge at LEO-15 and that it is the forcing mechanism for ripple migration.

4.2. Bedload Modeling

Since bedload or near-bottom suspended transport was not measured directly, to test the hypothesis that it is forcing ripple migration, one can compare the sediment transport associated with the migration of the ripples to sediment transport predicted by a bedload model. Dimensionless bedload flux (Φ_B) models typically take a form of

$$\Phi_B = C_B(|\theta_w^{sf}| - \theta_{crit})^{1.5}\frac{\theta_w^{sf}}{|\theta_w^{sf}|} \quad \text{if} \quad |\theta_w^{sf}| > \theta_{crit}$$
$$\Phi_B = 0 \quad \text{if} \quad |\theta_w^{sf}| < \theta_{crit} \tag{28}$$

where dimensionless bedload flux is defined as

$$\Phi_B = \frac{Q_B}{\rho_s D\sqrt{gD(s-1)}} \tag{29}$$

and Q_B is the bedload flux in g/cm s, θ_w^{sf} is the wave skin friction Shields parameter, θ_{crit} is the critical Shields parameter (θ_c=0.04), and C_B is a constant of proportionality. The quantity $|\theta_w^{sf}| - \theta_{crit}$ is the excess Shields parameter above the critical threshold. The well-tested (for flat beds, and steady flow) *Meyer-Peter and Muller* [1948] formula suggests use of (28) with C_B=8. To extend this type of formula to spectral waves with nonzero skewness *Nielsen* [1992] suggests using

$$\theta_w^{sf}(t) = \frac{1}{2}\frac{f_{2.5}\sqrt{2}u_{w,\,rms}u_w(t)}{gD(s-1)} \tag{30}$$

to calculate an instantaneous Shields parameter. In (30), $f_{2.5}$ is calculated on the basis of H_{rms} for a burst, and the wave period calculated by (4). A zero degree phase lag between stress and velocity is also assumed. Since $u_w(t)$ are the instantaneous wave velocity samples within a burst, (30) generates a time series of instantaneous Shields parameters within the wave cycle. From the time samples of instantaneous Shields parameter within the bursts the cumulative bedload transport is calculated as

$$M_{bedload}(t) = \sum_0^t Q_B(t)\frac{\Delta T_b}{T_b}\Delta t \tag{31}$$

$M_{bedload}$ is compared to the sediment transport associated with ripple migration (M_{ripple}) in Figure 15a. In order to make the magnitude of $M_{bedload}$ agree with M_{ripple} over the period yearday 238 to 260 a scaling factor of C_B=8 × 62 was used instead of the 8 suggested by the *Meyer-Peter and Muller* [1948] formula. While *Nielsen* [1992] recommended the use of $\sqrt{2}u_{w,\,rms}u_w(t)$, based on the rms wave height, for the velocity-squared factor in (30) other possibilities exist. Table 1 shows the required scaling constants for the velocity-squared factor based on the rms wave height, the significant wave height, and the actual instantaneous wave velocity. The motivation for using the instantaneous wave velocities is from *Madsen* [1991], who suggested bedload responds virtually instantaneously to time varying velocities associated with waves. The fact that the scaling constants are substantially larger than 8 indicates that either scaling for this type of bedload formula needs to be substantially larger for the bedload transport associated with orbital scale ripple migration, or that a significant portion of the transport is occurring as near-bottom suspended load.

Table 1. Velocity-Squared Factors and the Associated Bedload Model Scaling Constants.

Wave Height Definition	Velocity-squared factor	C_B
H_{rms}	$\sqrt{2}u_{w,\,rms}u_w(t)$	8×62
$H_{1/3}$	$1.42\sqrt{2}u_{w,\,rms}u_w(t)$	8×21
Instantaneous	$u_w(t)$	8×10

Another possibility for the difference in the magnitude of transport between the data and the model with C_B=8 is that there is velocity enhancement as the flow passes over the crest of the ripple. This type of velocity enhancement is particularly important when the wave stresses are near the critical stress for initiation of motion. However, if sediment is in motion only near the crest, there exists a trade-off in increased bedload transport due to the increased flow velocity and in decreased bedload transport due to the spatial average over the ripple wavelength. If sediment is in motion over the entire face of the ripple the flow enhancement at the crest is balanced by flow speed reduction over the trough and the spatially averaged transport rate does not increase substantially.

Nielsen [1992], on the basis of data from *Du Toit and Sleath* [1981], suggested a velocity enhancement factor of $1/(1-\pi\eta/\lambda)$ based on velocity measurements over orbital scale vortex ripples. Thus the enhanced Shields parameter is given by

$$\frac{\theta_w^{sf}}{(1-\pi\eta/\lambda)^2} \tag{32}$$

Using this Shields parameter and the original model scaling constant of C_B=8 gives an $M_{bedload}$ that agrees well with M_{ripple}. This calculation does not account for the reduction in bedload transport due to spatial averaging over a ripple wavelength and thus overestimates $M_{bedload}$. The use of a flow enhancement factor is also not universally agreed upon in the literature. *Wiberg and Harris* [1994], on the basis of measurements by *Ikeda* [1991], suggested that a flow enhancement factor should only be used for anorbital ripples. In a recent paper, *Li et al.* [1997] used this flow enhancement factor to predict initiation of bedload motion over a rippled bed.

Comparing Figure 15a (M_{ripple} and $M_{bedload}$) to Figure 14a (Ripple migration X_m and $U3_w$), one can see there is better agreement of the shape of the curves in Figure 15a. This is due to the fact that while the shape of $M_{bedload}$ and $U3_w$ are similar, the ripple migration transports less sand during periods of slow migration when the ripples are small and more sand during periods of fast migration when the ripple are larger. This forces the slope of M_{ripple} to become steeper than the slope of X_m in the period around yearday 250 and flatter elsewhere. In general, the shape of curves M_{ripple} and $M_{bedload}$ agree well, thus this type of bedload model with the appropriate velocity squared factor and scaling constant can be used as a predictive tool for sediment transport associated with ripple migration in conditions similar to those found at LEO-15 during this deployment.

To test the possible role of bedload caused by mean currents, the bedload flux model calculations were also performed with the combined stress estimates generated using the GGM model for the stress due to currents and (30) for the stress due to waves. In Figure 15 it is shown that the model results for the combined case and for waves alone are virtually identical indicating that the contributions from mean currents is negligibly small.

The fact that the ripple migration is onshore and is forced by bedload and near-bed suspended transport, and that the suspended sand transport above 5 cm off the bottom is offshore during the period of largest waves can be interpreted in terms of a vortex ejection process as described by *Bagnold* [1946], *Inman and Bowen* [1963], *Nielsen* [1992], and others. Flow separation and vortex formation is occurring at LEO-15 as indicated by the sharp crested ripples (Figure 2.) High-frequency ABS images of plumes of suspended sediment rising to 60 to 80 cm above the bottom are also consistent with a vortex ejection process. One possible explanation of the observed phenomena is shown in Figure 17.

The observations of ripple migration directed onshore with suspended transport directed offshore (presumably carrying the finer fractions) are consistent with *Craghan's* [1995] observations of grain size distributions across Beach Haven ridge where the coarsest sediments are found on the landward flank and become progressively finer over the crest. This consistency assumes the ripple migration is forced by bedload and carries coarser sediments and the suspended transport consists of finer fractions as consistent with a vortex ejection mechanism.

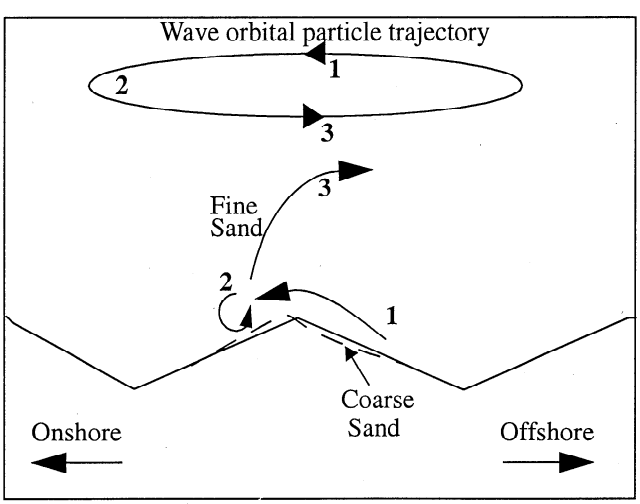

Figure 17. Vortex ejection and bedload forcing of ripple migration mechanism. The greatest velocities are in the onshore direction. This onshore portion of the wave cycle moves fine and coarse sand over the crest (1) where most of the coarse sand is deposited to force the ripple migration, as seen by the dashed line. This is the dominant cross-shore transport mechanism. However, some of this sand (particularly the finer fractions) that passes over the crest is entrained into a vortex in the lee of the ripple (2). This vortex is ejected upward into the water column during the wave reversal and is transported offshore in the next half of the wave cycle as it decays and sand settles out (3). The grain size dependence of this process is described by *Bagnold* [1946] and could account for the offshore suspended transport during periods of high wave velocity. While this process reverses every half wave cycle, the stronger onshore velocities associated with nonlinear waves allows the onshore phase to dominate.

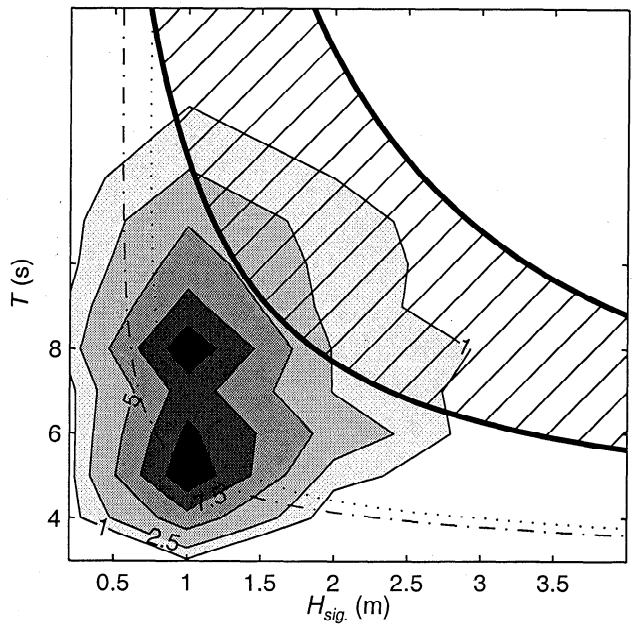

Figure 18. Annual significant wave height versus dominant period frequency of occurrence distribution from 9 years of *National Data Buoy Center* [1997] buoy 44009 hourly observations located at the mouth of the Delaware Bay in 30 m of water. The total area under the contours integrates to 100%, and contours are labeled in percent. The hatched area is the transitional region from wave orbital scale ripples to anorbital scale ripples defined with D=800 μm. The dash-dotted and dotted lines are the Shields critical limits for initiation of motion for grain sizes of 400 and 800 μm, respectively.

5. Wave Ripple Climatology for LEO-15

The data analyzed in this paper was taken over a 6 week period during an active hurricane season. Wave climatology can be used to examine whether the observed wave orbital ripples are the dominant type of bedform at LEO-15 in other seasons or over a longer timescale. Data of this type is readily available from the *National Data Buoy Center*'s [1997] wave buoy 44009 located in 30-m depth water at the mouth of the Delware Bay approximately 100 km south of LEO-15. Figure 18 displays the frequency of occurrence distribution versus wave period and significant wave height taken from 56,788 hourly records during a 9-year period from October 1984 to December 1993. Also plotted on this figure is the Shields critical stress threshold for initiation of motion for the observed median grain size of D_{50}=400 μm and one standard deviation larger (D_{85}=800 μm). The transitional region (2000 < d/D < 5000) from wave orbital scale ripples to anorbital ripples based on wave orbital diameter scaled by a grain size of D_{85}=800 μm is shown as the hatched region. A scaling based on D_{85} is used since this scaling predicts a transition from orbital ripples to anorbital ripples that is not inconsistent with the observations from LEO-15. The critical stress is found from the wave height and period by using linear wave theory to find velocities. The 2.5 grain diameter wave friction factor ($f_{2.5}$) is used to relate velocity to skin friction shear stress.

By integrating the part of the frequency of occurrence distribution that lies above the critical stress it is seen that 74% of the observations fall into this category based on a grain size of 400 μm. Thus stresses are typically large enough to form wave orbital ripples that are in equilibrium with wave forcing. By integrating the part of the distribution that lies above the lower limit of the transitional region it is seen that 18% of the observations fall into this category. In our data set, 90% of the points lie above the critical stress and only 2% are in the transitional region defined with a grain size of 800 μm

Thus if a transition occurs, it will only happen in the more severe storms at LEO-15. Although our deployment occurred during an active tropical storm season, all of these storms passed well offshore of the LEO-15 site, generating long-period swell but not locally large waves. The dominant periods of the waves during the most severe event in the deployment were 16-18 s, but the significant heights were rarely over 2 m. A winter or late fall deployment would be more likely to catch the severe northeast wind storms that would generate locally large waves. Such a deployment could help determine whether the maximum observed ripple wavelength of 100 cm is truly the maximum wavelength possible before a transition to anorbital scaling occurs, or whether the ripples can grow longer than 100 cm. The wave climatology indicates that until further information is available on the transition to anorbital scaling, a wave orbital scale ripple model is valid at LEO-15 for a large percentage of the time.

6. Conclusions

Wave orbital scale ripples with λ/d_s=0.74 and η/λ=.15 are clearly the dominant type of bedform observed at LEO-15. The only exception to this is during periods when the current stress becomes significant relative to the wave stress (i.e., $\tau_c^{sf}/\tau_w^{sf} \sim O(1)$) or during periods when the bedforms are not in equilibrium with the wave forcing. Although it is unclear whether a transition to anorbital ripple scaling is occurring, models such as those by *Clifton and Dingler* [1984] and *Wiberg and Harris* [1994], with the transition occurring at d/D~2000 and with D defined by the median grain size (D_{50}) do not predict this data set well since this transition predicts a maximum wavelength of 45 cm while the maximum observed wavelength is 100 cm. Scaling the relation d/D by a grain size one standard deviation above the median (D_{85}) allows the model to predict the maximum observed wavelength of 100 cm before a transition occurs. This indicates that scaling these types of models by median grain size alone may not be appropriate and some measure of the width of the grain size distribution should be included. In the case of LEO-15 the presence of the larger grains allowed the ripples to grow larger than the model predicted. Models such as those by *Nielsen* [1992] or *Grant and Madsen* [1982] that use wave period are able to predict the correct maximum wavelength, even when scaled by the median grain size. Collecting data during severe winter storms with large wave orbital diameters would help clarify the issue of an orbital-anorbital transition. Also, collecting data grain size distribution spatial variability across ripples crest and troughs, along with formulating detailed models of the relative roles of suspended sediment and bedload in the ripple formation process, may help determine the appropriate scaling for a transition. A laboratory study with narrow and wide grain size distributions with the same median size and varying wave period with constant orbital diameter could also

help clarify the roles of grain size distributions and wave period on ripple geometry.

Although understanding bedform geometry is important for its effect on near-bed hydrodynamics and thus the sediment transport process, the migration of ripples may be the dominant mode of cross-shore sediment transport at a site such as LEO-15 with medium to coarse sand. If the assumption that the volume of sand contained in the ripples is transported with the ripple is correct, then the ripple transport accounts for an order of magnitude more mass transport than the net suspended transport. Transport models are able to relate this mode of sand transport with a forcing function related to (excess stress)$^{1.5}$ with an appropriate scaling constant. Better instrumentation is needed to carefully measure bedload and near-bottom suspended transport and to relate these transport modes to ripple migration. The observations indicate a process where ripples migrated onshore yet suspended sediment travels offshore during storms. Vortex ejection is a possible mechanism for this transport pattern, but it should be emphasized that while the existing observations are consistent with this hypothesis, high-resolution two- or three-dimensional observations are required to better understand these processes.

Acknowledgments. The authors would like to thank Scott Glenn and Richard Styles at Rutgers University for making the BASS data available and the Rutgers University Marine field station and WHOI staff for assistance with the deployment. This work was supported by NOAA New York Bight Research Center grant NA46GU0149 and ONR grant. N00014-97-1-0556. WHOI contribution 9796.

References

Amos, C.L., A.J. Bowen, D.A Huntley, and C.F.M. Lewis, Ripple generation under the combined influences of waves and currents on the Canadian continental shelf, *Cont. Shelf Res., 8*(10), 1129-1153, 1988.

Bagnold, R.A., Motions of waves in shallow water; Interaction between waves and sand bottoms, *Proc. R. Soc. London, Ser. A, 187*, 1-15, 1946

Boyd, R., D.L. Forbes, and D.E. Heffler, Time-sequence observations of wave-formed sand ripples on an ocean shoreface, *Sedimentology, 35*, 449-464, 1988.

Carstens, M.R., F.M. Nielsen, and H.D. Altinbilek, Bed forms generated in the laboratory under an oscillatory flow: analytical and experimental study, *Tech Memo 28*, 39 pp., U.S. Corps of Eng., Coastal Eng. Res. Cent., Washington, D.C., 1969.

Clifton, H.E., Wave-formed sedimentary structures: A conceptual model, in *Beach and Nearshore Sedimentation*, edited by R.A. Davis, Jr. and R.L. Ethington, *SEPM Spec. Publ.*, 24, 126-148, 1976.

Clifton, H.E., and J.R. Dingler, Wave-formed sedimentary structures and paleoenvironmental reconstruction, *Mar. Geol., 60*, 165-198, 1984.

Craghan, M., Topographic changes and sediment characteristics at a shoreface sand ridge- Beach Haven Ridge, New Jersey, M.S. thesis, 123 pp., Rutgers Univ. New Brunswick, N.J., 1995.

Dingler, J.R., Wave-formed ripples in nearshore sands, Ph.D. thesis, 136 pp., Univ. of Calif., San Diego, 1974.

Du Toit, C.G., and J.F.A. Sleath, Velocity Measurements close to rippled beds in oscillatory flow, *J. Fluid Mech., 112*, 71-96, 1981.

Duane, D.B., M.E. Field, E.P. Meisburger, D.J. Swift, and S.J. Williams, Linear shoals on the Atlantic Inner Continental Shelf, Florida to Long Island, in *Shelf Sediment Transport,: Process and Pattern*, edited by D.J. Swift, D.B. Duane, and O.H. Pilkey, chap. 22, 447-498, Van Nostrand Reinhold, New York, 1972.

Engelund, F., and J. Fredsoe, Sediment ripples and dunes, *Annu. Rev. Fluid Mech., 14*, 13-37, 1982.

Fredsoe, J., and R. Deigaard, *Mechanics of Coastal Sediment Transport*, World Sci., River Edge, N.J., 1992.

Grant, W.D., and S.M. Glenn, *Continental shelf bottom boundary layer model, vol. 1, Theoretical model development*, Woods Hole Oceanogr. Inst., Woods Hole, Mass., 1983.

Grant, W.D., and O.S. Madsen, Combined wave and current interaction with a rough bottom, *J. Geophys. Res., 84*, 1797-1808, 1979.

Grant, W.D., and O.S. Madsen, Movable bed roughness in unsteady oscillatory flow, *J. Geophys. Res., 87*, 469-481, 1982.

Hay, A.E., and D.J. Wilson, Rotary sidescan images of nearshore bedform evolution during a storm, *Mar. Geol., 119*, 57-65, 1994.

Horikawa, K., *Nearshore Dynamics and Coastal Processes: Theory, Measurement, and Predictive Models*, Univ. Tokyo Press, Tokyo 1988.

Ikeda, S., K. Horikawa, and K. Noguchi, Oscillatory boundary layer over a sand ripple model, *Coastal Eng. Jpn., 34*, 15-29, 1991.

Inman, D.L., Wave generated ripples in nearshore sands, *Tech Memo 100*, 66 pp., U.S. Army Corps of Eng., Beach Erosion Board, Washington, D.C., 1957.

Inman, D.L., and A.J. Bowen, Flume experiments on sand transport by waves and currents, in *Coastal Engineering, Proceedings of the 8th Conference.*, pp. 137-150, Am. Soc. Civ. Eng., New York, 1963.

Irish, J.D., J.F. Lynch, P. Traykovski, and A.E. Newhall, A self contained sector scanning sonar for bottom roughness observations as part of suspended sediment studies, *J. Atmos. Ocean Technol.*, in press, 1998.

Komar, P.D., Oscillatory ripple marks and the evaluation of ancient wave conditions and environments, *J. Sedimentary Petrol., 44*(1), 169-180, 1974.

Lee Young, J.S., and J.F.A. Sleath, Ripple formation in combined transdirectional stead and oscillatory flow, *Sedimentology, 37* 509-516, 1990.

Li, M.Z., C.L. Amos, and D.E. Heffler. Boundary layer dynamics and sediment transport under storm and non-storm conditions on the Scotian Shelf, *Mar. Geol., 141*, 157-181, 1997.

Longuet-Higgins, M.S., On the statistical distribution of the height of sea waves,. *J. Marine Res., 11*, 245-266, 1952.

Lynch, J.F., J.D. Irish, C.R. Sherwood, and Y.C. Agrawal, Determining suspended sediment particle size information from acoustical and optical backscatter measurements, *Cont. Shelf Res. 14*(10/11), 1139-1165, 1994.

Madsen, O.S., Mechanics of cohesionless sediment transport in coastal waters, *Coastal Sediments '91 proceedings*, pp. 15-27, Am. Soc. Civil Eng, 1991.

Madsen, O.S. and W.D. Grant, Sediment Transport in the Coastal Environment, *Rep. No. 209*, Ralph M. Parsons Lab., Mass. Inst. of Technol., Cambridge, MA., 1976.

Madsen, O.S., and P.N. Wikramanayake, Simple models for turbulent wave current bottom boundary layer flow, *Contract Report DRP-91-1*, U.S. Army Corps of Eng., Coastal Eng. Res. Cent., Dredging Res. Program, Vicksburg, Miss., 1991.

Madsen, O.S., Y. K. Poon and H.C. Graber, Spectral Wave Attenuation by Bottom Friction: Theory, in *Coastal Engineering, Proceedings of the 21st Conference.*, Vol. 1, pp. 492-504, Am. Soc. Civ. Eng., New York, 1988.

Meyer-Peter, E. and R. Muller, Formulas for bedload transport, paper presented at International. Association for Hydraulic Structural Research, Stockholm. 1948.

Miller, M.C. and P.D. Komar, Oscillation sand ripples generated by laboratory apparatus, *J. Sediment. Petrol., 50*(1), 173-182, 1980a.

Miller, M.C. and P.D. Komar, A field investigation of the relationship between oscillation ripples spacing and the near-bottom water orbital motions, *J. Sedimen. Petrol., 50*(1), 183-191, 1980b.

Mogridge, G.R. and J.W. Kamphuis, Experiments on bedform generation by wave action, *Coastal Engineering, Proceedings of the 13th Conference.*, pp. 1123-1142, Am. Soc. Civ. Eng, New York, 1972.

National Data Buoy Center, Climate Summary Tables, Feb. 1995, Stennis Space Center, Miss., 1997.

Nielsen, P. *Coastal Bottom Boundary Layers and Sediment Transport.* World Sci., River Edge, N.J., 1992.

Nielsen, P., Dynamics and geometry of wave-generated ripples, *J. Geophys. Res., 86*, 6467-6472, 1981.

Sheng, J., and A.E. Hay, An examination of the spherical scatterer approximation in aqueous suspensions of sand, *J. Acoust. Soc. Am., 83*(2), 598-610, 1988.

Sleath, J.F.A. *Sea Bed Mechanics*, John Wiley, New York, 1984.

Sternberg, R., Predicting initial motion and bedload transport of sediment particles in the shallow marine environment, in *Shelf Sediment Transport: Process and Pattern*, edited by D.J.P. Swift, D.B. Duane, and O.H. Pilkey, pp. 447-498, Van Nostrand Reinhold, New York, 1972.

Swart, D.H., Offshore sediment transport and equilibrium beach profiles, *Publ. 131*, Delft Hydr. Lab., Delft, Netherlands, 1974.

Wiberg, P.L., and C.K. Harris, Ripple geometry in wave-dominated environments, *J. Geophys. Res., 99*, 775-789, 1994.

Wheatcroft, R.A., Temporal variation in bed configuration and one-dimensional roughness at the mid-shelf STRESS site, *Cont. Shelf Res.*, 14(10/11), 1167-1190, 1994.

Wikramanayake, P.N, and O.S. Madsen, *Tech. progress rep. 2*, Calculation of Movable Bed Friction Factors, U.S. Army Corps of Eng. Coastal Eng. Res. Cent., Dredging Res. Program, Vicksburg, Miss., 1990.

Williams, A.J., J.S. Tochko, R. L. Koehler, W.D. Grant, T.F. Gross, and C.V. Dunn, Measurement of turbulence in the oceanic bottom boundary layer with an acoustic current meter array, *J. Atmos. Oceanic Technol.* *4*(2), 1987.

A.E. Hay, Department of Oceanography, Dalhousie University, Halifax, NS B3H 4J1, Canada. (hay@phys.ocean.dal.ca)

J.D. Irish, J.F. Lynch, and P. Traykovski, Department of Applied Ocean Physics and Engineering, Woods Hole Oceanographic Institution, Woods Hole, MA 02543. (jirirsh@whoi.edu; jlynch@whoi.edu; ptraykovski@whoi.edu)

(Received June 5, 1997; revised March 25, 1998;
accepted September 2, 1998.)